Experiments in Fluids (2024) 65:148
https://doi.org/10.1007/s00348-024-03882-1

RESEARCH ARTICLE

Determination of unsteady wing loading using tuft visualization

Francis De Voogt[1] · **Bharathram Ganapathisubramani**[1]

Received: 10 June 2024 / Revised: 30 August 2024 / Accepted: 8 September 2024 / Published online: 27 September 2024

Abstract

Unsteady separated flow affects the aerodynamic performance of many large-scale objects, posing challenges for accurate assessment through low-fidelity simulations. Full-scale wind tunnel testing is often impractical due to the object's physical scale. Small-scale wind tunnel tests can approximate the aerodynamic loading, with tufts providing qualitative validation of surface flow patterns. This investigation demonstrates that tufts can quantitatively estimate unsteady integral aerodynamic lift and pitching moment loading on a wing. We present computational and experimental data for a NACA0012 wing, capturing unsteady surface flow and force coefficients beyond stall. Computational data for varying angles of attack and Reynolds numbers contain the lift coefficient and surface flow. Experimental data, including lift and moment coefficients for a tuft-equipped NACA0012 wing, were obtained at multiple angles of attack and constant Reynolds number. Our results show that a data-driven surrogate model can predict lift and pitching moment fluctuations from visual tuft observations.

1 Introduction and literature

Tufts can be utilized for unsteady surface flow to approximate the instantaneous local flow direction near the object's surface. Each type of tuft has a specific drag, inertia, and stiffness which affects the response to the flow. Furthermore, the specific application method of tufts on a surface can also influence their ability to indicate the local flow direction (Chen et al 2019). These and other shortcomings have largely precluded the use of tufts to obtain quantitative data. Surface flow visualization is typically used to compare and validate simulations with experiments (Neves et al 2020; Cai et al 2018). Still, some investigations have shown that tufts can be used to obtain quantitative flow field measurements. Tufts have been used for the identification of separated flow behind a backward-facing step where also the frequencies of the tuft fluctuations are considered (Chen et al 2020). Similarly, tufts have been used in studies to characterize the flow on full-scale wind turbines, for which the stall fraction is of interest (Vey et al 2014; Swytink-Binnema and Johnson 2016). These studies showed the ability of tufts, combined with a camera and image processing, to achieve a reliable quantitative estimate of a desired parameter in operational conditions. More detailed quantitative information has been obtained from tufts, by using them to obtain velocity fields or identify pressure fluctuation based on the deflection of tufts (Steinfurth et al 2020). This investigation also indicated some issues associated with tufts in flow regions with low flow velocity or high-frequency flow oscillations.

For stalled wings, there can be significant unsteady surface flow, leading to unsteady aerodynamic loading. Wings with airfoil profiles that exhibit trailing edge stall characteristics have a tendency to develop coherent surface flow patterns after stall (Broeren and Bragg 2001). These characteristic flow patterns typically consist of a curved separation line along the spanwise direction, which is terminated at both ends by two vortices on the wing surface (Moss and Murdin 1968). This flow structure is often referred to as a stall cell. An example of a stall cell surface flow configuration is shown in Fig. 1, based on findings by Manolesos et al (2014a), Manolesos et al (2014b) and Yon and Katz (1998). The criteria for the formation of stall cells have been shown to be dependent on the airfoil shape, the angle of attack, and the Reynolds number (De Voogt and Ganapathisubramani 2022; Dell'Orso and Amitay 2018; Schewe 2001). The exact formation mechanism for stall cells has not been shown yet but has been reasoned to be related to the Crow-like instability in combination with a spanwise disturbance on the two shear layers due to the separated flow (Crow 1970; Weihs

✉ Francis De Voogt
f.devoogt@soton.ac.uk

Bharathram Ganapathisubramani
g.bharath@soton.ac.uk

[1] Aeronautical and Astronautical Engineering, University of Southampton, University Road, Southampton, UK

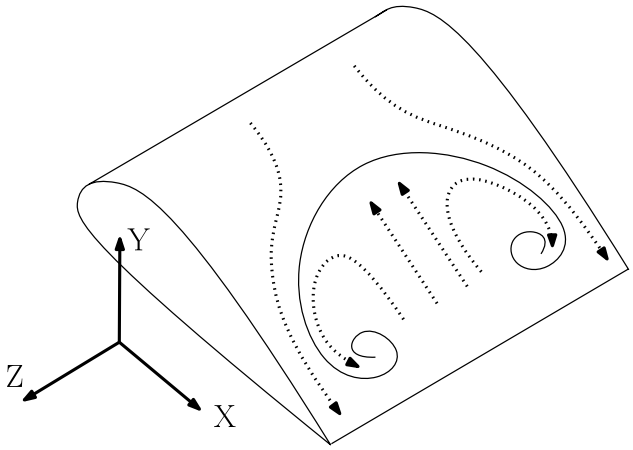

Fig. 1 Flow direction (dotted lines) near the wing surface inside and outside of a stall cell

and Katz 1983). The influence of a stall cell on the wing loading has been shown to be similar to a locally decreased effective angle of attack near the center of a stall cell (Yon and Katz 1998). At this spanwise location, the flow near the surface has an upstream direction. Previous investigations have shown that the presence of stall cells on a wing influences the wing performance significantly (Liu and Nishino 2018). One investigation showed that time-averaged measurements of a wing with the same airfoil profile produced different results for the lift coefficient after stall (Bartl et al 2019). This difference in measured lift coefficient has been attributed to multiple factors, including the presence of stall cells, or the lack thereof. Similarly, the unsteady behavior of stall cells has been shown through CFD simulations to be highly related to the fluctuations in the lift coefficient of the wing (Liu and Nishino 2018). Stall cells can form on the surface of many aerodynamical bodies, resulting in fluctuating aerodynamic loading.

Many local stall patterns can emerge, each with distinctive surface flow characteristics that significantly influence aerodynamic performance. Using a data-driven approach, we can correlate these visual surface flow patterns with aerodynamic loading effects. For research purposes, it is crucial to link surface flow behaviors to fluctuations in wing loading, thereby enhancing our understanding of the impact of separated surface flow patterns. In practical applications affected by separated flow, such as in automotive aerodynamics, establishing a relationship between observable surface flow on an object and the challenging-to-measure unsteady aerodynamic loading is highly beneficial. This underscores the necessity of developing a data-driven surrogate model to accurately capture this relationship.

The angle of attack and Reynolds number significantly influence a wing's aerodynamic performance, determining regimes like attached or separated flow. Simplistic surrogate models struggle to estimate unsteady aerodynamic loading from these steady input parameters. In this investigation, visual tuft observations are utilized as dynamic inputs for a surrogate model to estimate unsteady lift and moment coefficients. In Sect. 2, the methodology for a data-driven surrogate model that estimates the unsteady wing loading from visual tuft observations is explained. In Sect. 3, this approach has been evaluated on ideal data obtained with CFD simulations. The goal of the CFD investigation is to establish if it is possible to determine the lift fluctuations from near-surface flow patterns. In Sect. 4, the data-driven surrogate model approach has been tested on noisy experimental data. The experimental data have also been used to test the extrapolation abilities of the data-driven surrogate model approach. Finally, in Sect. 5 the conclusions of the current investigation are summarized.

2 Data-driven model for unsteady loading from tufts

In this section, the data-driven surrogate model approach is described for the lift coefficient fluctuations. This approach has also been used for the moment coefficient fluctuations.

The angle of attack and the Reynolds number are the primary parameters to determine an estimate of the steady lift coefficient of a given wing. When using unsteady data, it is common practice to take the average result from multiple instantaneous measurements at a fixed angle of attack and Reynolds number to obtain a representative steady lift coefficient result. This approach is shown by Eq. (1) with n measurements for a given $\alpha - \mathrm{Re}$ combination, where the over-line indicates the average for the lift coefficient.

$$\overline{C_L}(\alpha, \mathrm{Re}) = \frac{\sum_{i=1}^{n} C_{L,i}(\alpha, \mathrm{Re})}{n} \Big|_{\alpha, \mathrm{Re}\,=\,\mathrm{constant}} \tag{1}$$

Unsteady tufts can be used as inputs to a simple surrogate model to produce an estimate for the corresponding unsteady lift coefficient. Tufts can be assumed to be straight lines at an angle in a 2D plane observed by a camera. The angle of the tufts can vary from 0 to 2π radians. When a tuft is near the 0 - 2π boundary, the value for the angle can change significantly for small changes in tuft orientation. This non-physical discontinuity may adversely affect the performance of a data-driven model. In order to avoid the 0– 2π numerical boundary in the data, the tufts orientations have been encoded with both the sine and cosine of the tuft angles. Each tuft can thus be represented by two values in a range from -1 to 1. These values representing the tuft orientations

serve as the inputs for the data-driven model. The unsteady component of the lift coefficient (ΔC_L) can be represented as a deviation from the steady lift coefficient. In Eq. (2), the linear combination of the steady and the unsteady lift coefficient components is shown, with a function of the tufts $\mathcal{F}$(tufts) representing the unsteady component.

$$C_L = \overline{C_L}(\alpha, \mathrm{Re}) + \mathcal{F}(\text{tufts}) \tag{2}$$

It has been chosen to utilize a simple neural network, for $\mathcal{F}$(tufts). A neural network has the ability to learn complex input patterns while dealing with potentially noisy input data. Due to the limited amount of training data available, it is preferred to keep the amount of trainable parameters in the model small. Additionally, to speed up training and reduce the need for hyperparameter tuning, it is preferred to limit the amount of hidden layers. A neural network with two hidden dense layers has been used. The first hidden layer has 100 nodes and the second has 10 nodes. This architecture allows for an order of magnitude reduction in the number of trainable parameters per layer to reach the single parameter output. ReLU activation functions for the hidden layers were found to converge faster to the final error than sigmoid activation functions during training. However, the sigmoid activation functions converged to a lower final loss than the ReLU activation functions. As such, it was chosen to use sigmoid activation functions for the hidden layers. Two dropout layers are used, one between the input and the first hidden dense layer, and a second dropout layer is used between the first and the second hidden dense layers. These dropout layers have been used to limit the potential of the network to be overly reliant on a limited set of tufts to produce the output, the randomized dropout promotes the use of a large combination of tufts in the neural network. The use of dropout layers increases robustness of the network with respect to the imperfect flow direction estimation of the tufts. The full network architecture is shown in Fig. 2. The inputs to the network are the sine and cosine of the tufts on the wing surface and the output is the magnitude of the instantaneous lift fluctuation. A network with the same architecture can be constructed but trained with the pitching moment as an output. The L2 norm between the known output values of the training set and the model estimation has been minimized in combination with the ADAM optimizer (Kingma and Ba 2014). The computational data consider 260 tufts, resulting in 520 inputs for the neural net. The experimental data consider 55 tufts, resulting in 110 inputs for the neural network. This difference in the number of inputs introduces more trainable parameters for (the first layer of) the neural network used with computational data. A different neural network is created for the computational lift coefficient, experimental lift coefficient, and experimental pitching moment coefficient.

To effectively train a data-driven model, it is essential to have a comprehensive dataset. This dataset should contain exact unsteady wing loading output values, derived from either CFD simulations or wind tunnel experiments, for corresponding tuft orientation inputs. Such a foundational dataset enables the model to learn the underlying surface flow patterns and their statistical relation to unsteady wing loading.

Once the data-driven model has been trained, various elements can be tested to assess its capabilities and limitations. One inherent limitation is that tufts do not provide flow velocity information, which may limit the models' performance in some cases. This issue may be significant when dealing with geometrically similar surface flow patterns that differ in velocity. By incorporating comprehensive training data, the model may learn sufficient variations in surface flow patterns, enabling it to interpolate between these

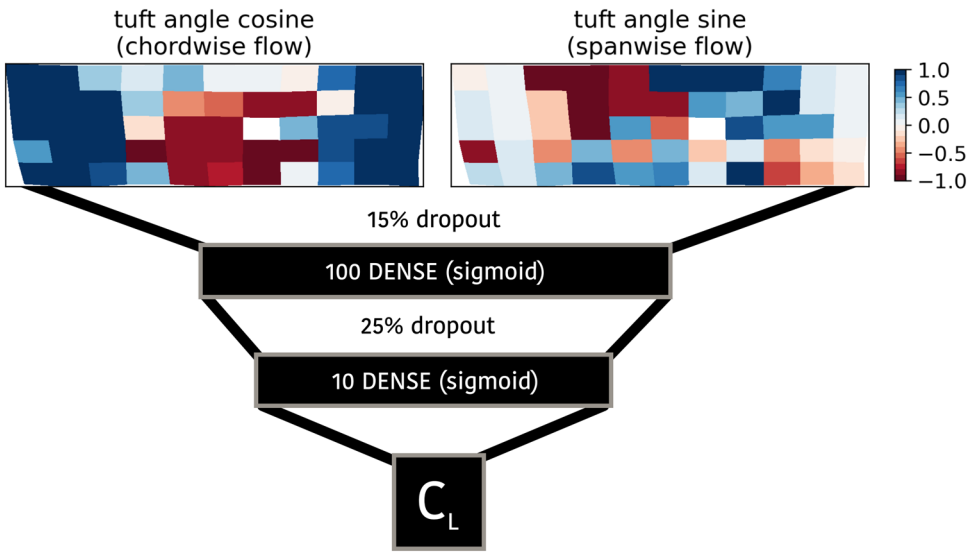

Fig. 2 A two layer neural network architecture for determining the lift or pitching moment fluctuations from 55 experimental tufts. The same architecture is used for the computational data with 260 tufts

variations and estimate the aerodynamic loading effects of surface flows not explicitly included in the training data.

Some of these challenges can be tested using CFD data, which is largely free from noise, with clearly defined surface flow patterns and minimal small-scale unsteady separated flow patterns. A single model (for ΔC_L) has been trained on the majority of this data, spanning a range of angles of attack and Reynolds numbers. Surface flow regimes (trailing edge separation, stall cell, and full separation) differ based on these parameters. For some angles of attack and Reynolds numbers, the regimes might be similar, though geometric variations in the surface flow pattern (such as size and position) can still exist. The model's performance is tested on various angles of attack and Reynolds numbers not in the training data, specifically examining two conditions with flow separation.

The experimental data introduces challenges for a data-driven model due to physical constraints and noise. In the current experimental setup, fewer tufts have been used on the physical wing model compared to the computations, and various forms of noise can affect the data, such as external influences on measurements, response of tufts to flow as well as tufts becoming stuck. While the computational data mainly included small variations of surface flow patterns within three separated flow regimes, the experimental data present a broader range of less clearly defined surface flow patterns. This variability tests the model's ability to interpolate between diverse surface flow patterns. The experimental models, one for ΔC_L and one for ΔC_M, were trained on surface flow and aerodynamic loading fluctuations at a single angle of attack and a constant Reynolds number. By evaluating these models on different angles of attack, not included in the training data, it can be assessed whether the model's interpolation of surface flow patterns can effectively support its extrapolation to new conditions.

3 CFD demonstration

3.1 Setup

For the current investigation, a NACA0012 airfoil profile has been used with a 1-m chord length (c). A C-shaped mesh grid has been used which extends 15 chord lengths to the circular inlet section from the airfoil leading edge, and 15 chord lengths to the outlet. A 2D configuration of the NACA0012 profile has been used to assess the required number of circumferential mesh nodes for Unsteady Reynolds Averaged Navier Stokes (URANS) simulations. The lift coefficient has been evaluated for different meshes at three different angles of attack (5°, 10° and 15°) at a chord based Reynolds number of 10^6. The Reynolds number in this investigation refers to the chord-based Reynolds number defined as $\mathrm{Re} = \frac{u_\infty \cdot c}{\nu}$, where u_∞ is the freestream velocity, c is the chord length and ν is the kinematic viscosity of air at 15°C ($\nu = 14.61 \cdot 10^{-6}\ \frac{Ns}{m^2}$, $\rho = 1.225\ \frac{kg}{m^3}$). The resulting lift coefficients are shown in Table 1.

The mesh with 420 circumferential nodes was found to provide a suitable balance between accuracy and computational cost for the 3D URANS simulations. A detailed view of the mesh with 420 circumferential nodes around the airfoil is shown in Fig. 3a. The wall normal distance from the airfoil surface has been set to $8 \cdot 10^{-6}$ m for the wall adjacent nodes, such that $y^+ < 1$ for wall adjacent nodes at a Reynolds number of 10^6.

The 2D mesh with 420 circumferential nodes has been extruded in spanwise direction for 2.5 chord lengths to obtain a spanwise uniform wing with an aspect ratio (AR) of 2.5. In Fig. 3b, the full domain is shown for the 3D configuration. The spanwise mesh spacing (Δz) is 0.1 c; this allows for the formation of stall cells based on the findings of (Liu and Nishino 2018). The wing surface has been set as a smooth non-slip wall. Periodic boundary conditions have been used for the sidewalls of the domain; the inlet has been defined by the Cartesian velocity components for each $\alpha-$Re combination, and the outlet uses an average static pressure condition. The fluid domain has been initialized with the freestream velocity components. The turbulence intensity was zero at the location of the airfoil.

A shear stress transport turbulence model has been used with automatic wall functions in ANSYS CFX 18.1. A high resolution advection scheme in combination with high resolution turbulence numerics and a second order backward Euler transient scheme was used for the URANS solver. The time step size was set to 0.001 s, this is significantly smaller than the timescale of interest for the analysis. The investigation of (Liu and Nishino 2018) did not find an influence of the time step size on the results of the simulations. The convergence criterion for the RMS residuals was set to 10^{-5}, with a maximum of 15 coefficient loops per time step. The results of the simulations have only been saved every 0.1 s to limit the size of the data output. Simulations have been

Table 1 2D mesh convergence study

Circumferential nodes	C_L at $\alpha = 5° / 10° / 15°$
240	0.529 / 1.012 / 1.353
360	0.527 / 1.013 / 1.355
420	0.527 / 1.015 / 1.369
480	0.527 / 1.015 / 1.364
720	0.527 / 1.017 / 1.372

The resulting lift coefficient for three different angles of attack when using meshes with varying amounts of circumferential nodes on the airfoil surface

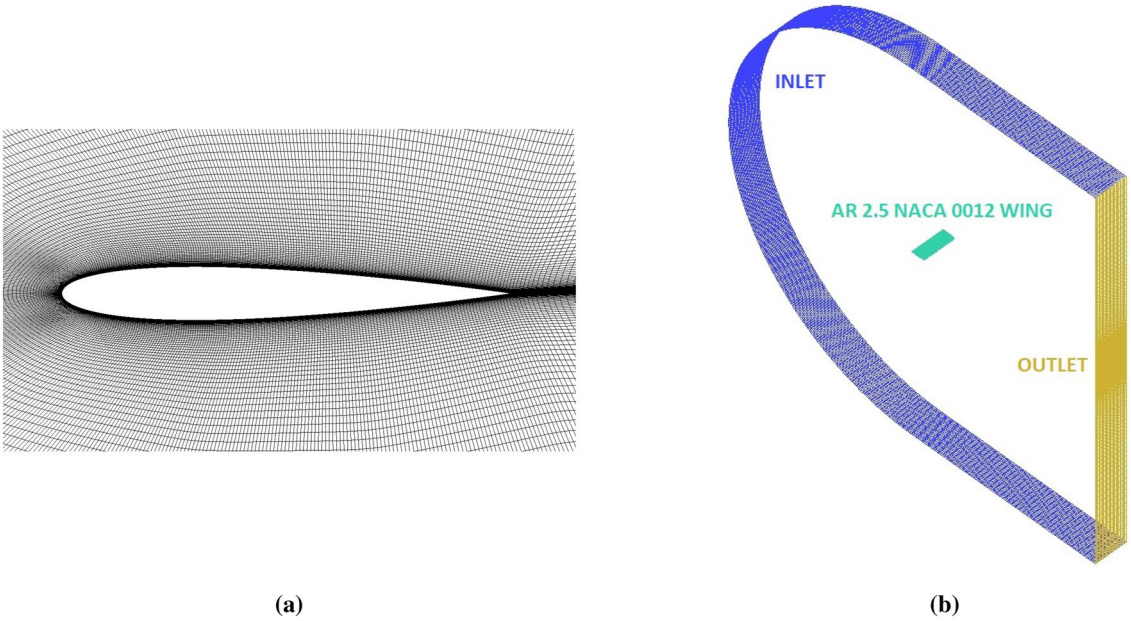

Fig. 3 The computational domain of the NACA0012 wing: **a** detail of the mesh around a NACA0012 profile and **b** the boundaries of the 3D C-grid. Periodic boundary conditions are applied to the sides of the domain which are not shown

run for 10–20 s of simulated time, depending on the flow case, to obtain a statistically representative time frame for the flow case.

For validation of the results, a comparison of the time-averaged lift coefficient (excluding the transient phase at the start of the simulation) is presented in Fig. 4. The spanwise spacing of the mesh grid can influence the flow patterns that occur on the wing post stall (and thus lift), as such these are also mentioned (Liu and Nishino 2018). The use of different solvers and other small differences can lead to differences in the resulting lift coefficient values; however, all presented investigations in Fig. 4 find the maximum lift coefficient at an angle of attack of 16 degrees. Beyond stall the $C_L - \alpha$ curve of the current investigation (for $\mathrm{Re} = 10^6$) falls within the range determined by different investigations.

Pseudo tufts were obtained by sampling the local flow at an offset of 0.001 c from the wing surface. In chordwise direction, 10 pseudo tufts were sampled between 0.05 x/c and 0.95 x/c at 0.1 c intervals. In spanwise direction, pseudo tufts have been sampled at 0.1 c intervals to match the original mesh grid spacing, an example is shown in Fig. 5.

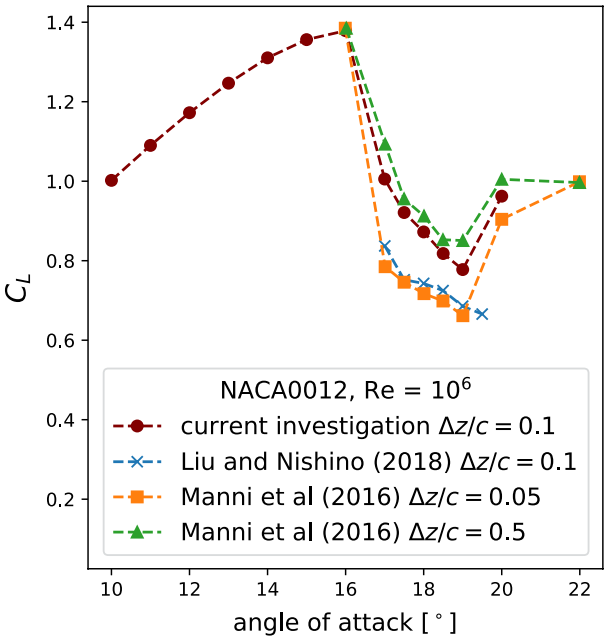

Fig. 4 Comparison of the lift coefficient obtained from CFD at a Reynolds number of one million from different investigations and with different spanwise spacing of the mesh grid. Data for validation used from Manni et al (2016) and Liu and Nishino (2018)

3.2 Observed surface flow

The use of periodic boundary conditions allows to simulate an infinite wing. The investigation by (Liu and Nishino 2018) presents in great detail the effect of the AR of the wing in combination with periodic boundary conditions. As previous investigations indicated that the NACA0012 airfoil profile tends to produce stall cell patterns of approximately 2.5 c in spanwise width, the current investigation uses a wing with AR 2.5 (De Voogt and Ganapathisubramani 2022; Moss and Murdin 1968; Gregory and O'Reilly 1970; Manni

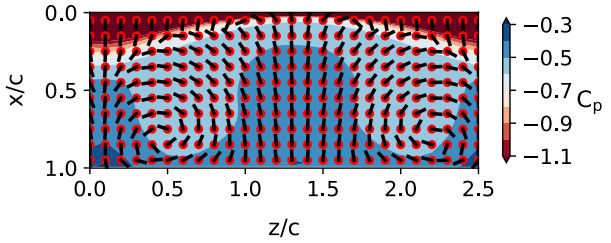

Fig. 5 Visualization of pseudo tufts with pressure coefficient contours for angle of attack 18° and Re = 10^6 (time = 8.5 s). The freestream direction is from the top of the image to the bottom

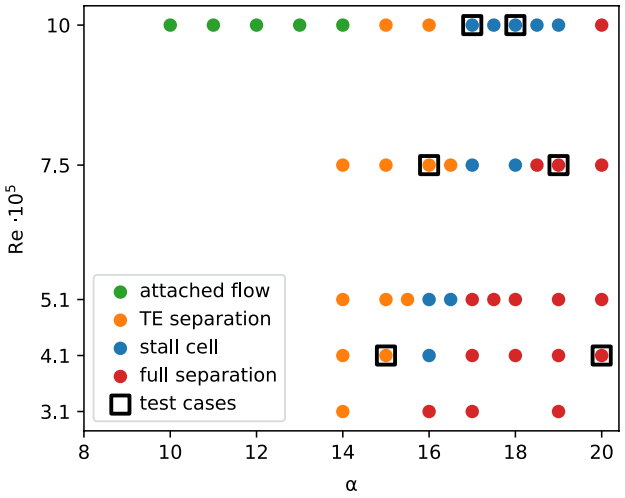

Fig. 7 All α − Re combinations that have been computationally simulated for a NACA0012 wing with AR 2.5 and periodic boundary conditions

et al 2016). By varying the angle of attack and Reynolds number over a wide range around and beyond stall, multiple flow configurations have been observed, as shown in Fig. 6.

For attached flow, there is no upstream flow observable. Trailing edge separated flow shows upstream flow near the trailing edge, without the presence of vortices near the wing surface. Stall cell flow patterns contain two vortices on the wing surface and upstream flow between them. Lastly, full separation represents upstream flow over the entire wing surface. Most α − Re combinations that have been simulated contain some form of flow separation. Separated flow often results in unsteady flow behavior and by extension an unsteady lift coefficient for a constant α − Re combination. All 43 distinct α − Re combinations which have been simulated are shown in Fig. 7.

For the highest Reynolds number under consideration, 10^6, the widest range of angles of attack has been simulated. This wide range for the angle of attack illustrates the four different primary flow configurations under consideration: attached flow, trailing edge (TE) separation, stall cells, and full separation. In Fig. 8, examples are shown for the lift coefficient results of two cases which contain stall cells at an angle of attack of 17° with two distinct Reynolds numbers. During the first seconds of the simulated time (< 100 convective cycles), it can be seen that the flow and thus lift coefficient are adjusting, and the lift coefficient does not yet represent the characteristic oscillatory behavior that is associated with unsteady stall cell flow (Liu and Nishino 2018).

From the range of simulated α − Re combinations, it can be observed that the angle of attack range in which stall cells occur varies across the Reynolds numbers tested. More specifically, at higher Reynolds numbers, the range of angles of attack in which stall cells occur can be seen to be wider and occur at higher angles of attack in Fig. 7.

For both TE separation and full separation, the tufts tend to be aligned with the chord in either upstream or downstream direction. For TE separation and full

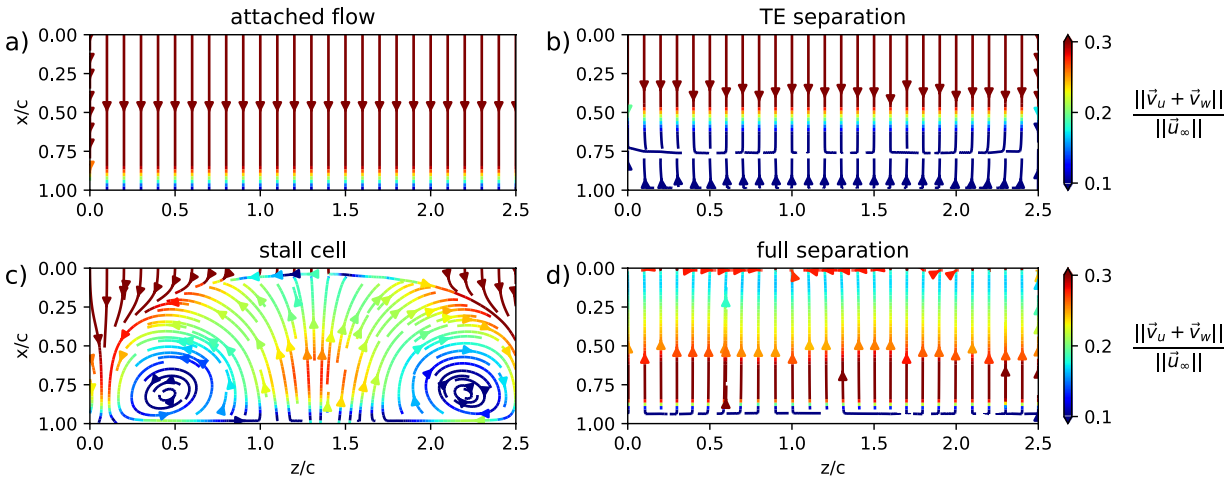

Fig. 6 Visualization of different surface flow patterns. All samples are at Re = 10^6 with **a** $\alpha = 10°$, **b** $\alpha = 16°$, **c** $\alpha = 18°$, and **d** $\alpha = 20°$

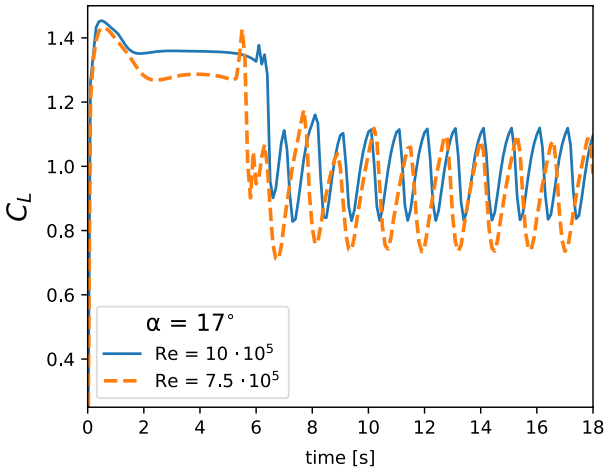

Fig. 8 The lift coefficient as obtained with URANS simulations for two cases with angle of attack 17° and two different Reynolds numbers. Both cases exhibit stall cell surface flow behavior

separation, the flow is mostly uniform along the span. For cases with stall cells present significant variation in flow direction near the wing surface along the span is induced by stall cell vortices, such as shown by Fig. 9. The surface flow can locally be observed to include also spanwise velocity components, as opposed to almost no spanwise surface flow for cases with TE separation or full separation.

3.3 Unsteady wing loading from tufts

To assess the ability of the data-driven method to generalize to other $\alpha - \mathrm{Re}$ combinations several cases have been selected to serve as test cases, these have been indicated with a black square in Fig. 7. Among the test cases are varying angles of attack, Reynolds numbers and the three surface flow configurations with separated flow which are of interest for unsteady wing loading. The training and test sets both exclude the initial 25% of the simulated time to eliminate the majority of the initial transient phase of the simulation. The training dataset contains 4631 snapshot samples representing 37 cases (unique $\alpha - \mathrm{Re}$ combinations), while the test set contains 731 samples representing six cases. The training − test split is thus approximately 86 − 14 (%), respectively, in terms of cases (and closely matched for sample count). For clarification with respect to the commonly used test-validation-train split for data-driven methods, the test set referred to in this investigation is a dataset that does not influence the training of any method, with the exception of determining the average lift coefficient for a given angle of attack and Reynolds number combination (Eq. (1)). All data used for training the neural networks are either a subset of the training dataset (validation set, used for early stopping criteria of the training) or the complete training dataset.

In Sect. 2, the model architecture has been described that is used to construct a surrogate model for the unsteady wing loading estimate based on the pseudo tufts. For this computational approach, the first step is to obtain a steady estimate

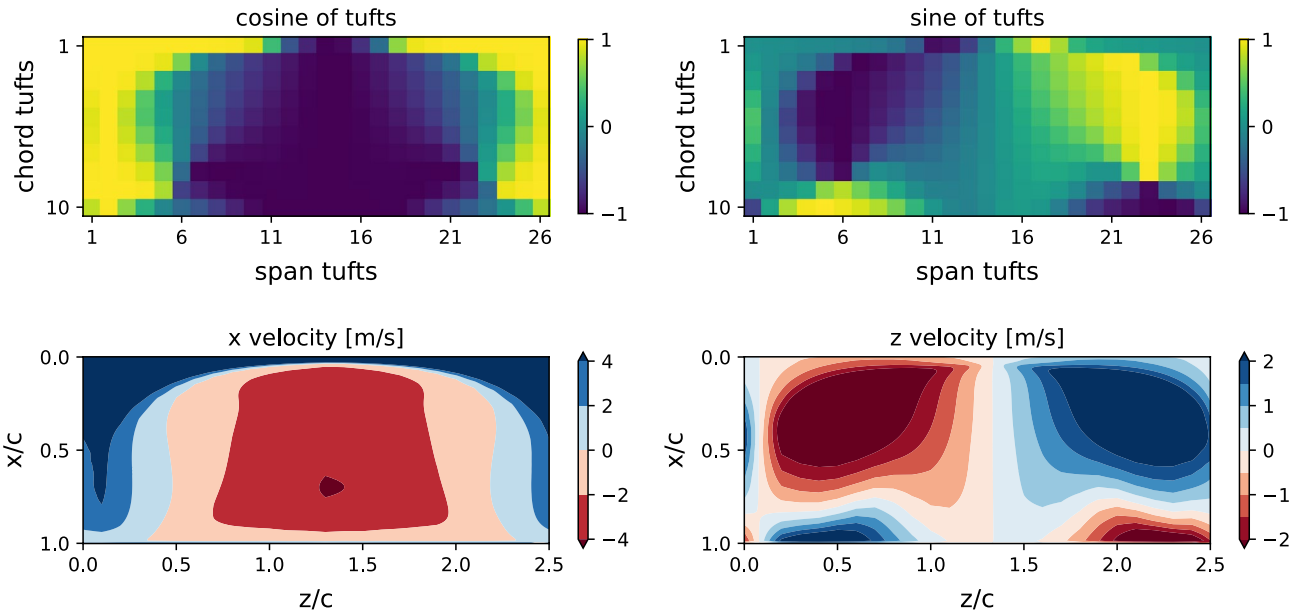

Fig. 9 An example of a stall cell in the computational URANS results. The cosine and sine of the pseudo tufts which have been obtained from the surface flow velocity (0.001 x/c offset from the surface) on the suction side of the wing, with x/c = 0 the leading edge of the wing, for angle of attack 18° and Re = 10^6 (time = 8.5 s)

for the wing lift coefficient for each α − Re combination, as shown in Fig. 10. For the calculation of the average lift coefficient per case, also the test cases have been taken into account, as no other suitable method would lead to a reasonable estimate for the average lift coefficient. Interpolating the known average lift coefficient based on known C_L values for different α − Re combinations can lead to large errors if not enough α − Re combinations are known. Alternatively, some other unrelated methods to obtain a steady estimate might exist such as 2D RANS or potential flow. These methods are computationally cheaper than 3D URANS, but come with other disadvantages such as limited accuracy for separated flow cases.

Using the cosine and sine of 260 pseudo tufts as inputs, the neural network has been trained to minimize the error for the corresponding instantaneous lift coefficient fluctuations. After training, the neural network model has been evaluated on the test cases. The output of the model is the deviation of the lift coefficient from the average value for a given angle of attack and Reynolds number. The average lift coefficient is added to the predictions of the model, the resulting lift coefficients of this evaluation are shown in Fig. 11 for the test cases. Looking at the lift coefficient for the different test cases, it can be seen that cases with stall cells or full separation produce unsteady lift. The two cases with TE separation on the wing surface (Re $= 7.5 \cdot 10^5$ with $\alpha = 16°$, and Re $= 4.1 \cdot 10^5$ with $\alpha = 15°$) show a steady lift coefficient. For the cases with TE separation, the orientation of the tufts is also steady, the steady input to the model produces a steady output. Since there are no lift coefficient fluctuations, the model correctly produces a steady output of approximately zero. Test cases with full separation on the wing surface (Re $= 7.5 \cdot 10^5$ with $\alpha = 19°$, and Re $= 4.1 \cdot 10^5$ with $\alpha = 20°$)

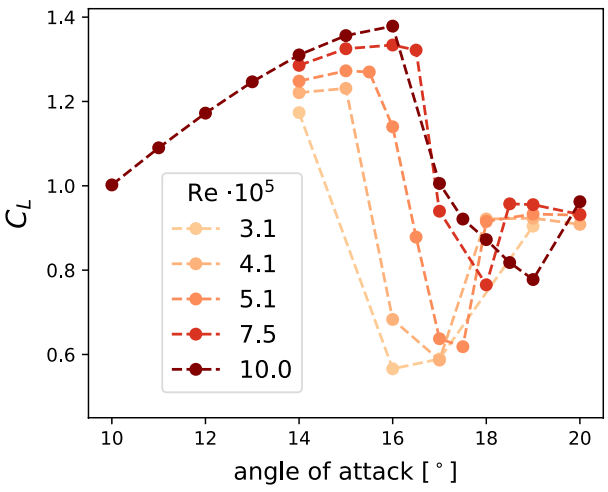

Fig. 10 The average lift coefficient obtained from the URANS simulations for each α − Re combination. The initial 25% of the simulated time is ignored to omit the transient phase

exhibit fluctuations with a single frequency peak in the frequency spectrum. This frequency peak is at a nondimensional frequency of approximately 0.3 for the Re $= 7.5 \cdot 10^5$ with $\alpha = 19°$ case and at approximately 0.55 for the Re $= 4.1 \cdot 10^5$ with $\alpha = 20°$ case. The lift coefficient fluctuations, as predicted by the surrogate model, for the cases with full separation contain the same frequency peak in the frequency spectrum as the original lift coefficient obtained with CFD. The tuft fluctuations for these cases are periodic, and as such so is the output for the lift coefficient fluctuations. Finally, the two cases with a stall cell on the wing surface (Re $= 10^6$ with $\alpha = 17°$, and Re $= 10^6$ with $\alpha = 18°$) show an unsteady lift coefficient. From the frequency spectra, it can be seen that the lift coefficient from CFD contains a primary frequency peak and then other smaller peaks at higher frequencies. For the case with Re $= 10^6$ with $\alpha = 17°$, the predicted lift coefficient fluctuations match the CFD results well as shown by the frequency spectra. The predicted lift coefficient fluctuations contain the same frequency peaks as the CFD lift coefficient. For the case with Re $= 10^6$ with $\alpha = 18°$, the predicted lift coefficient fluctuations do not match the CFD fluctuations well between 30 and 70 convective cycles. After 70 convective cycles, the frequency of the fluctuations for both the predicted and CFD lift coefficient fluctuations match well, as also illustrated by the frequency peak in the frequency spectrum. The initial mismatch between the signals for the early convective cycles causes an apparent low-frequency oscillation in the predicted signal, as can be observed in the frequency spectrum. With a single surrogate model, it is shown that the unsteady lift fluctuations can be estimated based on the tuft orientations. For a variety of surface flow configurations, with some form of flow separation present, the frequency content of the fluctuations can be accurately predicted. This evaluation on CFD data illustrates the ability of the surrogate model approach to be applicable to a wide range of angles of attack and Reynolds numbers, by interpolating between learned surface flow patterns.

4 Wind tunnel demonstration

4.1 Setup

The experiments were conducted in a wind tunnel at the University of Southampton, with a test section of 2.1 m by 1.6 m and 0.02 m/s accuracy for the set velocity. The free stream turbulence intensity has been measured along the wing leading edge, near the wind tunnel ceiling, this was found to be approximately 1%, and approximately 0.5% at the wing endplate. For the experimental setup, a wing with a NACA0012 profile, AR 2.6 and chord length of 30 cm was used. A schematic representation of the wing in the wind tunnel is shown in Fig. 12a. This wing was suspended

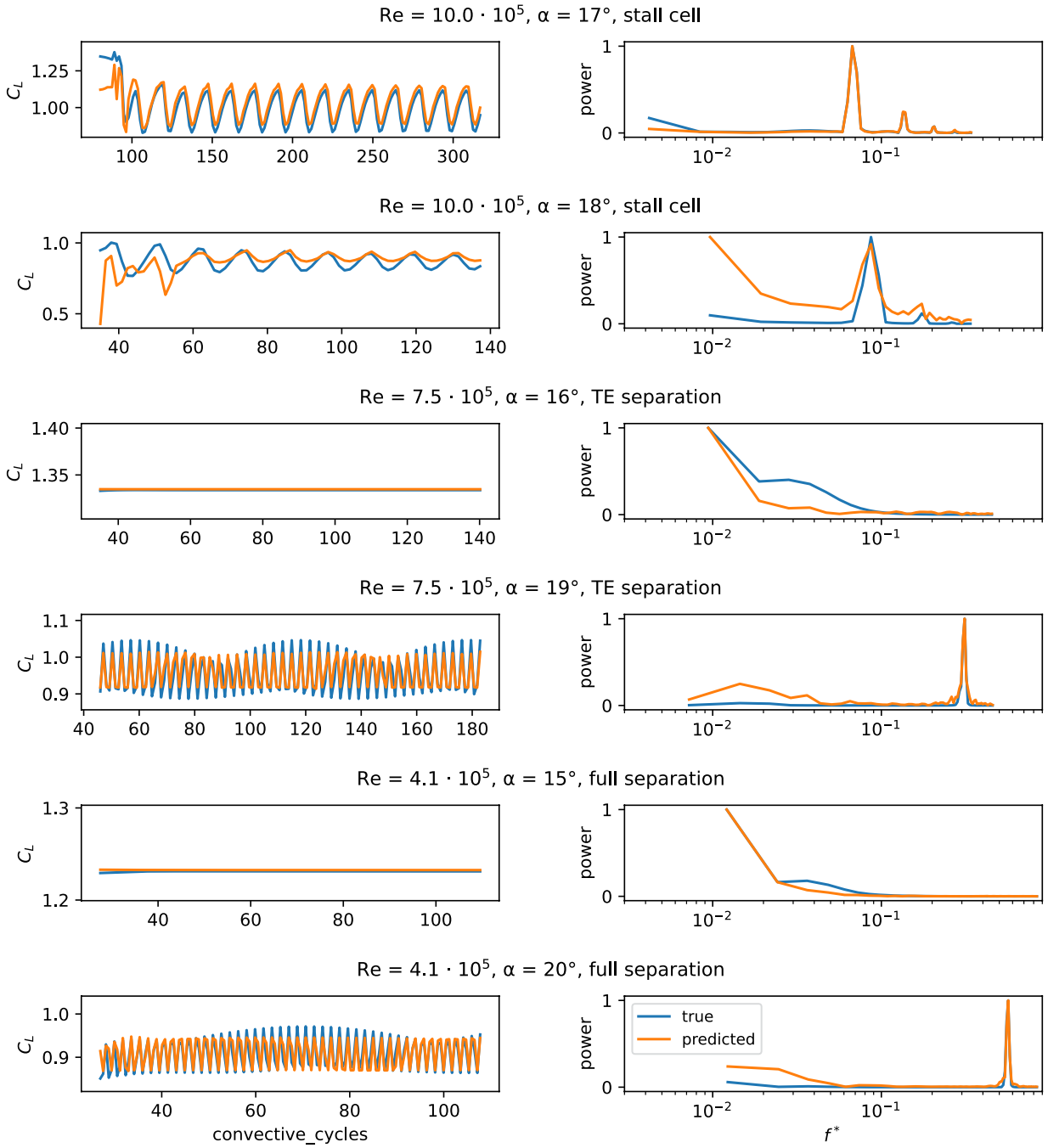

Fig. 11 The lift coefficient for the test cases obtained with CFD (blue) and the predicted lift coefficient from the surrogate model (orange) are shown on the left. The frequency spectrum of both signals is shown on the right

from an ATI Industrial Automation Delta IP65 force balance mounted outside the wind tunnel test section. An end plate was used, as shown in Fig. 12b, to limit the tip vortex effect. While the endplate is only partially effective at eliminating the tip vortex, the remaining effect of the tip vortex does not influence the determination of unsteady aerodynamic loading from tufts, as presented in this investigation. The wing was equipped with fluorescent tufts that were 5 cm long and less than 1 mm thick. In the chordwise direction, five tufts were used. In the spanwise direction, 13 rows of tufts were applied. In the analysis of the experimental data, the two outer rows of tufts (near the wind tunnel ceiling and the endplate) have been disregarded, leading to 11 rows of 5 tufts to be analyzed. The wing was illuminated with a UV floodlight. The tufts were recorded at 120 frames per second, with simultaneous force measurements at 6 kHz.

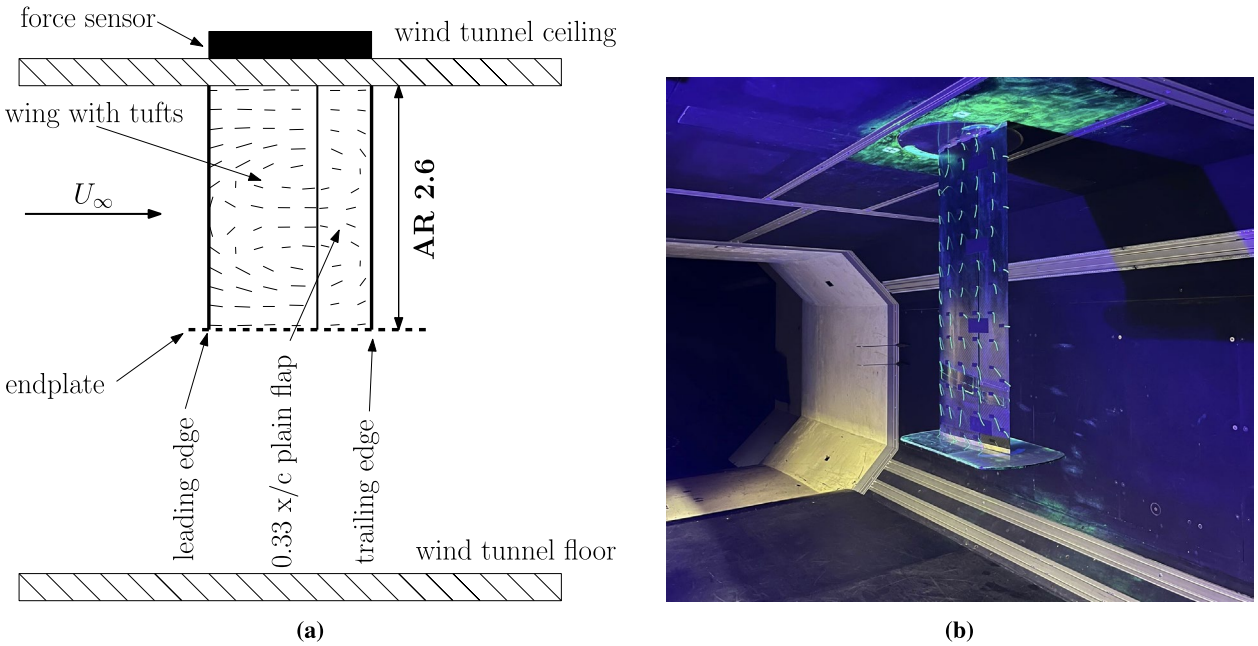

Fig. 12 The experimental setup of the NACA0012 wing equipped with tufts and a force balance: **a** A schematic of the setup and **b** the NACA0012 wing with fluorescent tufts and an end plate installed in the 7'x5' wind tunnel test section at the University of Southampton

4.2 Image processing

The tufts provide an estimation of the local flow angle near the surface of the wing. Using the sine and cosine values allows two continuous values to represent any angle. Additionally, the cosine and sine values represent the chordwise and spanwise flow directions, respectively, when zero radians is aligned with the freestream direction.

First, the captured images have been converted to black and white images, such that the tufts are clearly distinguishable from the background and each other. Some high reflection areas have been masked and a spanwise varying threshold has been used to obtain the black and white images as shown in Fig. 13.

The black and white images containing only tufts have been used in combination with a probabilistic Hough transform to obtain straight lines corresponding to the tufts, as shown in Fig. 14 (Galamhos et al 1999). The Hough transform allows to set certain parameters such as the line length, which should match the tuft length in the image or be slightly shorter. Hough lines located too far from known tuft locations have been eliminated. The remaining Hough lines have been grouped per tuft location by averaging the start- and endpoints of the Hough lines, to obtain a single Hough line per tuft location. In the final step, the endpoint of the Hough line closest to the known tuft fixed end location has been replaced by the known fixed end location. As is observable from Fig. 14, the last step of the process has almost no impact on the tuft identification when the image processing is suitable for the data. For 80.9% of the image samples, 52 or more tufts have been found, out of the 55 available tufts. In Table 2, the amount of samples per angle of attack with 52 or more tufts recognized are shown. At different angles of attack not only do the tufts behave differently, also the lighting conditions may vary slightly and the perspective of the camera relative to the wing changes slightly. These aspects can have an influence on the image processing, resulting in a different amount of tufts recognized on average per angle of attack.

From these identified tufts, the tuft angle can be obtained and converted into the corresponding sine and cosine values. Each sample thus has 55 values for the sine and 55 for the cosine (110 total values per snapshot image), missing tufts have a value of zero for both the sine and cosine.

In Fig. 15, the result of the image processing is shown. In the leftmost figure, the grayscale image is shown with the masked areas blacked out, the tufts as found by the image processing are shown on top in red. The second image from the left shows the amount of Hough lines found per tuft location and can be used to assess if the parameters of the probabilistic Hough line process are appropriate for the data from the current setup. The last two images on the right illustrate the sine and cosine of the tufts found for the shown sample.

4.3 Force and moment processing

Experimental measurements of the lift and pitching moments were taken at angles of attack 13°, 14°, 15°, 16° ,

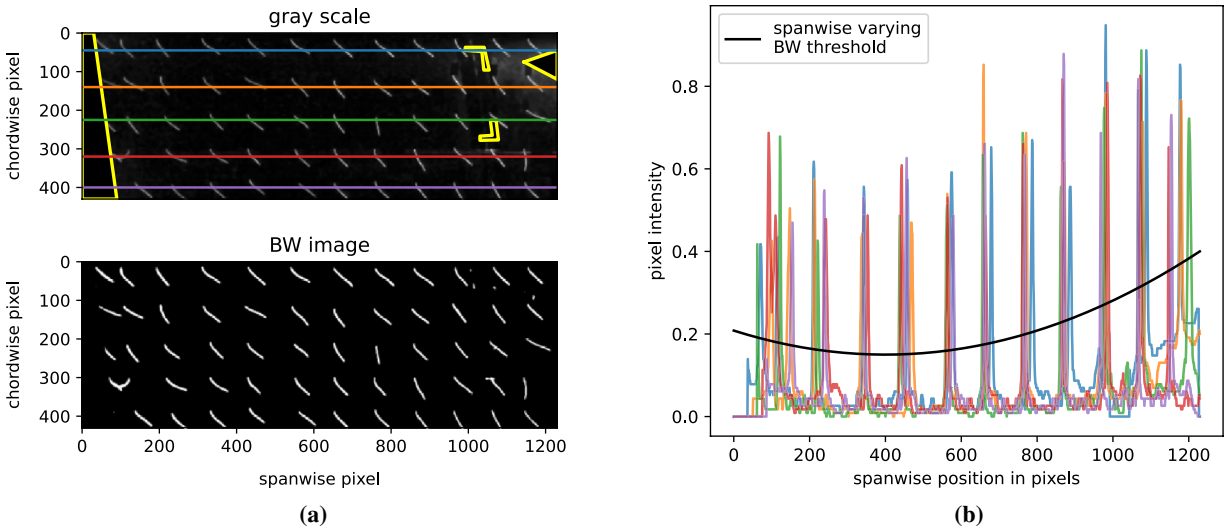

Fig. 13 Image processing of the tuft recording. **a** top: a single grayscale image, clipped to wing size, with masked areas indicated by a yellow circumference. The five horizontal lines crossing the tufts in spanwise direction indicate the locations of the analyzed pixel intensity in part **b**. **a** bottom: the resulting black and white image by using a spanwise varying threshold and masking. **b**: the intensity of the pixels crossed in a grayscale image as shown in the top image of part **a**

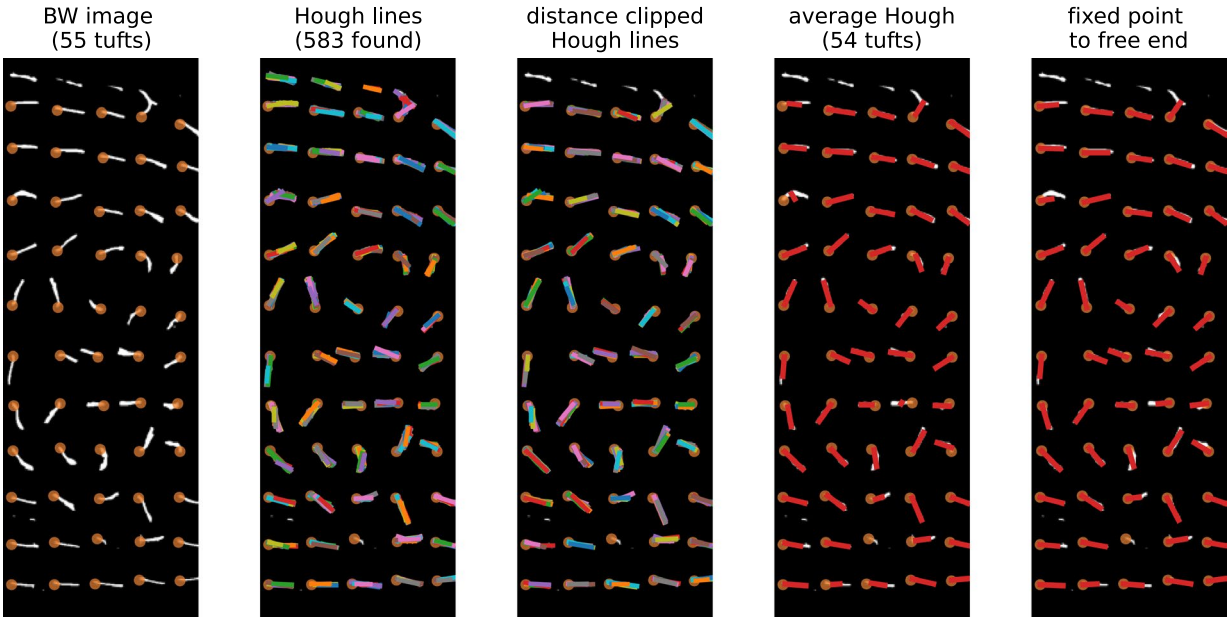

Fig. 14 Processing of the black and white images to obtain the tufts from each snapshot image. From left to right: identification of the fixed end of the tufts (orange dots), all Hough lines found, delete lines which are far away from the tuft fixed endpoints, average the begin and end points of the Hough lines grouped near a tuft fixed point and finally replace the Hough line starting point with the known tuft fixed end location

and 17°. The Reynolds number was constant at $2.0 \cdot 10^5$ for all angles of attack. The wind tunnel was stopped between testing different angles of attack. For the frequency analysis, we convert the measured frequency (f) to a nondimensional frequency (f^*) according to Eq. (3), where f is the measured frequency, c is the wing chord (0.3 m), and U_∞ is the freestream velocity (10 m/s).

$$f^* = \frac{f \cdot c}{U_\infty}, \tag{3}$$

Table 2 For each angle of attack and Reynolds number combination, the tufts on the wing behave differently, as a consequence the image processing does not provide consistent results across the range of angles of attack tested

Angle of attack	Amount of samples with 52 or more tufts recognized (%)
13°	94.2
14°	87.0
15°	71.5
16°	77.8
17°	73.8

The experimental data obtained with the force balance have a sampling frequency of 6 kHz ($f^* = 180$), while the camera used for recording the tufts used a frame rate of 120 Hz ($f^* = 3.6$). The experimental data used in this investigation considers only the time frame during which the aerodynamic forces are within nominal range for each angle of attack, eliminating the effects of the wind tunnel ramp up or down. Consecutive images of the tufts have been verified to have only very small differences in tuft orientations. It can be checked with the force and moment data if the frame rate of the tuft recordings is sufficient to capture the unsteady aerodynamic loading. This does not guarantee that the tufts are suitable for the investigated flow as they may react insufficiently to changes in the surface flow. A frequency analysis of the lift and pitching moment signal at 6 kHz is shown in Fig. 16. 125 Windows of 28.2 s have been used (total signal length is 3525 s, 705 s per angle of attack for five angles of attack), with Hanning weighting coefficients and no overlap (Bartlett's method) to obtain the frequency spectra (Nuttall 1981; Engelberg 2008). The large window size allows to analyze large timescale surface flow changes. The lowest measured frequency of 0.035 Hz in Fig. 16 corresponds to 940 convective cycles or a nondimensional frequency of $1.05 \cdot 10^{-3}$. The highest measured frequency of 3 kHz in Fig. 16 corresponds to 0.01 convective cycle or a nondimensional frequency of 90.

The frequency spectra show significant peaks at low f^* ranging between 0.001 and 0.01, showing the relevance of longer timescales. At a f^* of approximately 0.3, another significant peak in the lift and moment fluctuations frequency spectra can be observed in Fig. 16. It is expected that this frequency of force and moment oscillations represents the natural frequency of the suspended wing structure. This has not been verified. The angle of attack has been taken into account in the nondimensional frequency ($f^* \cdot sin(\alpha)$) to check if this large frequency peak collapses to a single nondimensional frequency for different angles of attack. This was found not to be the case, which reduces the likelyhood of this peak in the frequency spectra of the wing loading fluctuations to be of aerodynamic origin. The frequency spectra of several tuft locations for the angle of attack 13° have also been checked (both sine and cosine, representing spanwise and chordwise fluctuations, respectively), which

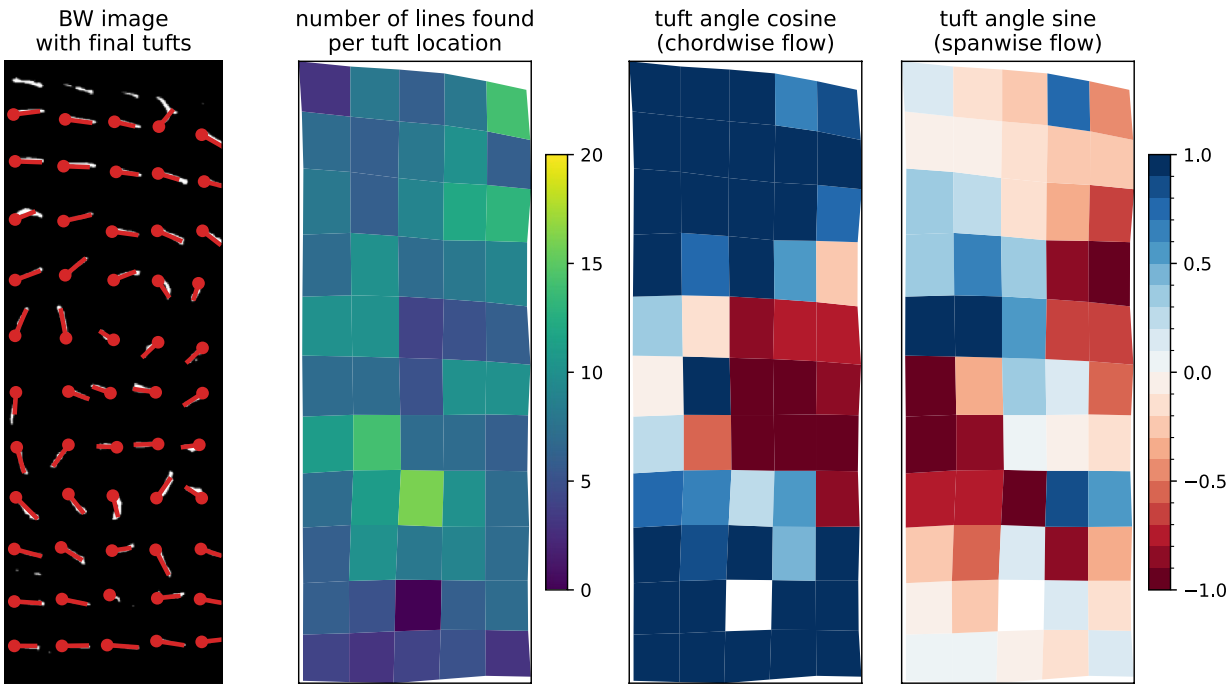

Fig. 15 The results from the image processing, from left to right: tufts found by the processing, tracking of the Hough process, map of the cosine of the tufts, and a map of the sine of the tufts. In the middle of the second tuft row from the bottom, a missing tuft can be observed

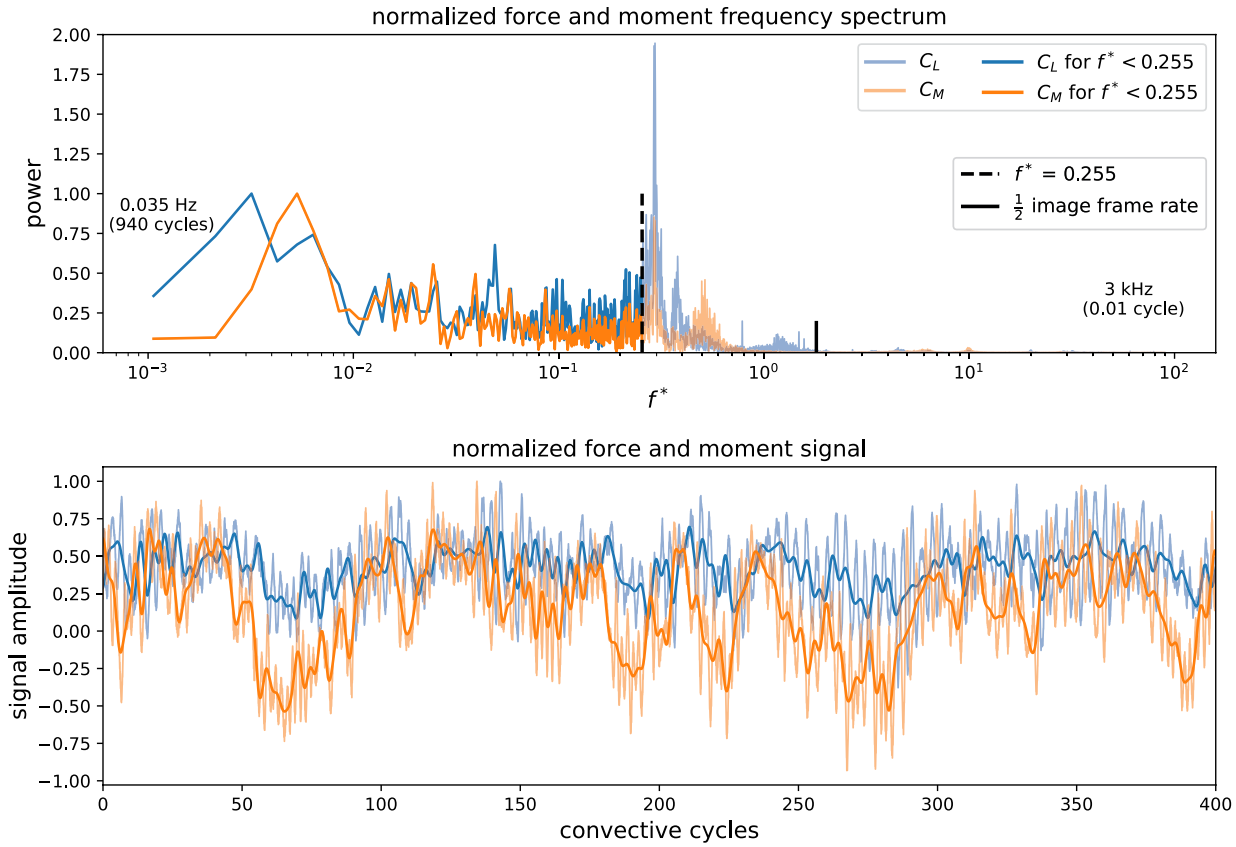

Fig. 16 Top: the frequency spectrum of the lift and pitching moment signal from all experimental data, normalized by the peak value of the 10 lowest f^*. Bottom: a sample of the signal acquired for the lift and pitching moment fluctuations, at angle of attack 13°, normalized by the highest absolute value per signal in the sample range

showed that the specific tuft location has a large influence on the frequency behavior of the tuft motions. More details are given in Sect. 5. To illustrate the lift and moment signal amplitude variation without the large amplitude of the natural frequency component, also a version of the signal, for angle of attack 13°, with all frequencies above $f^* = 0.255$ cut is shown in Fig. 16. The signals with a $f^* > 0.255$ cutoff are not used for the training of any model but have been used for interpretation of the results. The original lift and moment signals do not contain significant frequencies above a f^* of 1.8 (or 60 Hz), which is the tuft recording Nyquist frequency. For the data-driven model, the original force and moment measurements have been down-sampled to 120 Hz from 6 kHz, such that a corresponding lift force and pitching moment are available for each snapshot image of the tufts.

4.4 Observed surface flow

For each of the tested angles of attack, some form of flow separation was observed. In Fig. 17, snapshot images are shown of the tufts taken from the recordings of the wing, at different angles of attack in the wind tunnel. For angle of attack 13°, a patch of separated flow with a width of approximately half the wing span was observed to shift in spanwise direction multiple times per second. This patch of separated flow intermittently shows a stall cell structure. The surface flow for angle of attack 14° shows a larger patch of separated flow compared to angle of attack 13°. For angle of attack 14° a stall cell structure can consistently be observed. This stall cell occurs predominantly in the middle of the span but the stall cell position may also oscillate in spanwise direction. The stall cell width also was observed to fluctuate. Angle of attack 15° consistently shows a stall cell pattern that spans nearly the entire wing span. Angles of attack 16° and 17° show mostly a full span stall cell with intermittent full span turbulent separated flow.

4.5 Unsteady wing loading from tufts

The lift coefficient, pitching moment coefficient, and tufts have been acquired experimentally for five angles of attack (13° − 17°) of a NACA0012 wing at Reynolds number $2.0 \cdot 10^5$. For each angle of attack, there are 84,599 samples. For the experimental data, a consistent slight temporal

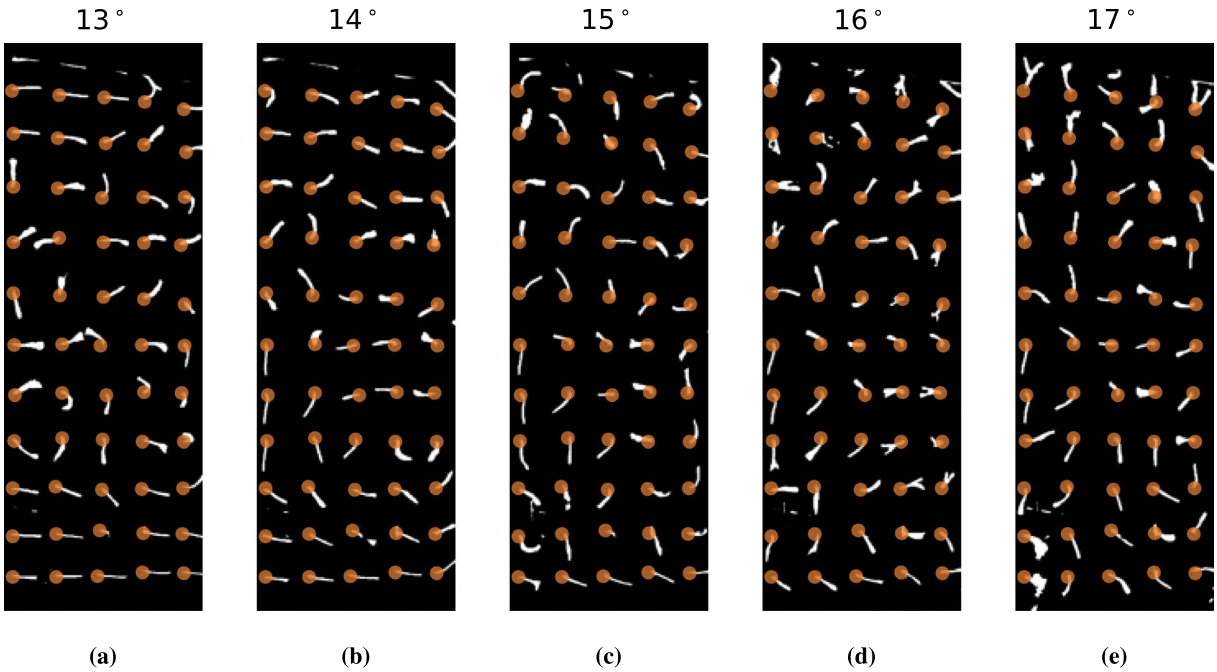

Fig. 17 Black and white images of the tufts at different angles of attack for a Reynolds number of $2.0 \cdot 10^5$. The freestream flow direction is from left to right in the images

offset between the lift and pitching moment was noticed, this has been corrected in the processing of all the experimental data by delaying the pitching moment by four image frames (0.033 s or approximately one convective cycle) relative to the lift. For the training of the surrogate models, a single angle of attack of 15° has been used. This angle is in the middle of the range of the available data. The mean of lift and pitching moment, obtained from the full angle of attack 15° dataset, has been subtracted from each, respectively. The models have been trained on the instantaneous lift and pitching moment fluctuations (ΔC_L and ΔC_M , respectively). For the model training, the validation dataset is a subset of the training data. The validation set is used to stop the training of the network when the validation data error does not improve for 100 epochs. The best version of the network, evaluated on the validation set during training, is restored. This version of the model is used to evaluate the test data. The last 20,000 samples in chronological order of the training data were chosen for validation, to improve the model generalization. The test data consider different angles of attack: 13°, 14°, 16° , and 17°. The test data have not influenced the training of the models. These angles of attack outside the training data range evaluate the models' ability to extrapolate to different angles of attack, with specific surface flow not present in the training data.

The tuft orientations of all samples for each angle of attack have been used as inputs for the surrogate models. The lift model outputs the predicted lift coefficient fluctuations and the moment model outputs the predicted pitching moment fluctuations. For the analysis of the results in the nondimensional frequency domain, 25 windows have been used for the data per angle of attack, with Hanning weighting coefficients and no overlap (Bartlett's method). The highest nondimensional frequency is given by the Nyquist frequency of the tuft recordings, which is 1.8. For each angle of attack, the power spectral density (PSD) is calculated for the predicted and measured lift fluctuations and the predicted and measured pitching moment fluctuations. The cross spectral density (CSD) has also been calculated for each measured signal with its corresponding predicted signal. For each angle of attack, the coherence can then be calculated as shown by Eq. (4), where C_α represents the coherence for angle of attack α.

$$C_\alpha = \frac{|CSD_\alpha|^2}{PSD_{\alpha,\text{predicted}} \cdot PSD_{\alpha,\text{measured}}} \tag{4}$$

The coherence can be calculated for either the lift or pitching moment coefficient fluctuations. The coherence value for a given frequency ranges from 0 to 1 and can be interpreted as a correlation between the two signals in the frequency domain at a given frequency, where 1 indicates that the signals are the same for that frequency, and 0 implies that they are completely unrelated.

In Fig. 18, the coherence is shown for all angles of attack for both the lift and pitching moment coefficient fluctuations.

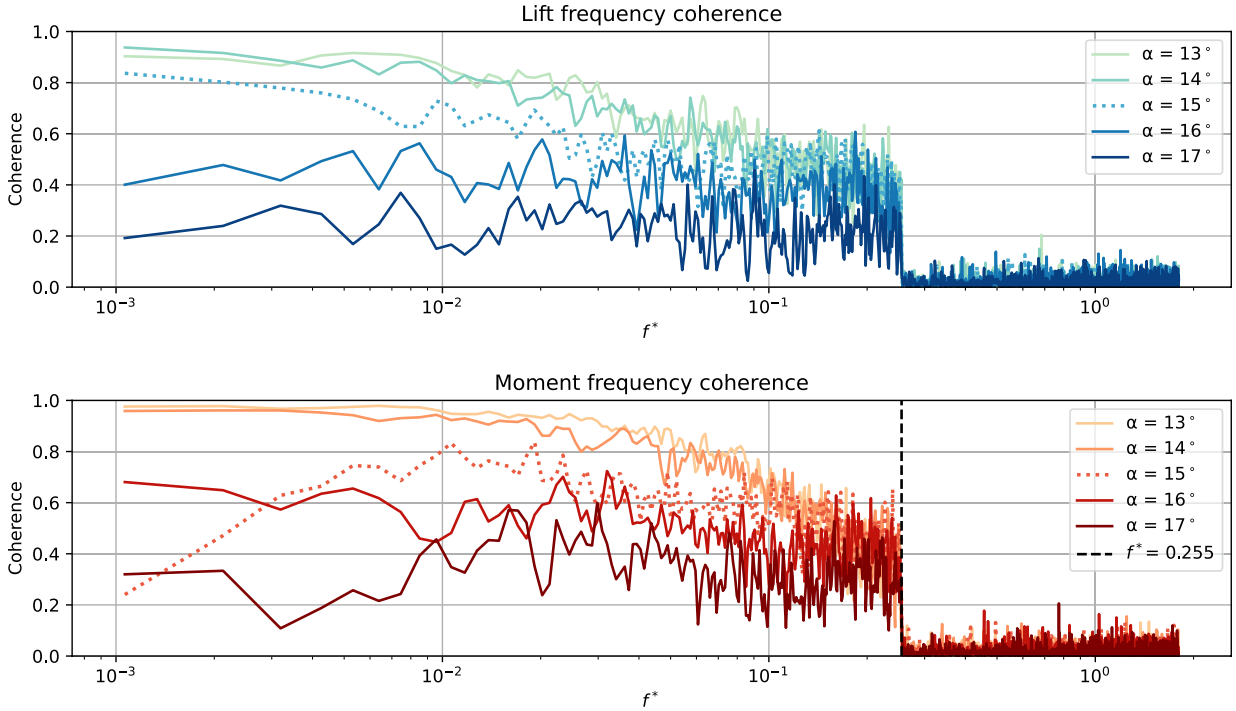

Fig. 18 The frequency coherence between the predicted signal and the experimentally measured signal, for both the lift and pitching moment. Angle of attack 15° represents the training data

For the lift coherence, it can be seen that for angles of attack 13° and 14° the predicted and measured signals are a very good match in the frequency domain for nondimensional frequencies below 0.01, with a coherence value of approximately 0.9. Beyond a f^* of approximately 0.1 the the coherence declines to a value of 0.4 approximately at $f^* = 0.255$. For angle of attack 15° , the coherence follows a similar trend as for angles of attack 13° and 14° across the range of frequencies, but with a constant reduction of approximately 0.1 in the coherence. For angles of attack 16° and 17°, the coherence is significantly lower over the range of frequencies below $f^* = 0.255$. For angle of attack 16° , the coherence hovers around 0.4 in this frequency range and for 17° the coherence hovers around 0.2 for this frequency range. This suggests that for these higher angles of attack the model may not necessarily capture the amplitude of the lift/moment fluctuations at the right level. Almost certainly, this is related to the complexity of flow mechanisms leading to the these fluctuations and the training data do not necessarily include this.

For nondimensional frequencies higher than 0.255, the coherence is very low and tends to be in the 0 to 0.1 range, indicating almost no relation between the predicted and measured signal in this frequency range. This drop-off in coherence coincides with the frequencies which contain the large PSD frequency peaks that were observed in the measured signals (as shown in Fig. 16), but not clearly observed in the tuft orientation dynamics. While the models were trained with the measured signal down-sampled to $f^* = 3.6$, the models do not accurately produce any fluctuations in the in the frequency domain with a f^* larger than 0.255. It is possible that either the tufts could not properly capture fluctuations higher than this frequency, or that these lift and moment fluctuations are not aerodynamic in nature. Similar observations can be made for pitching moment fluctuations. It can also be seen that the coherence tends to be higher in general in comparison with the lift coefficient coherence for individual angles of attack. For angles of attack 13° and 14° , the predicted and measured signals of the pitching moment coefficient fluctuations retain a high value for the coherence of approximately 0.9 for a wider frequency range than the lift coefficient fluctuations. For angle of attack 15° , the coherence for the lower frequencies below approximately 0.01 is lower than the coherence that was observed for the lift fluctuations at this angle of attack. For the angles of attack 16° and 17° the coherence for the pitching moment coefficient fluctuations is higher than for the lift coefficient fluctuations. These observations indicate that the models predict the coefficient fluctuations specifically well for lower angles of attack. Additionally, the lower frequencies tend to be predicted more accurately than the higher frequencies. It is also observed that the pitching moment coefficient fluctuations are predicted more accurately than the lift coefficient fluctuations in most cases.

The phase difference at each frequency is calculated by taking the angle of the (complex) cross-spectral density. This allows to investigate if the predicted signal is in phase with the measured signal for a range of frequencies. In Fig. 19, the resulting phase difference is shown for the experimental investigation. For both the lift coefficient and pitching moment coefficient fluctuations, it can be seen that the phase difference between the measured and predicted signal is close to zero for nondimensional frequencies lower than 0.01. For nondimensional frequencies between 0.01 and 0.2, the measured lift signal tends to lag the predicted lift signal, whereas for the pitching moment, the predicted signal tends to lag the measured signal. At a nondimensional frequency of 0.255, it can be observed that the phase shift appears to be random, this extends to the full 360° range outside the visible range in Fig. 19. Similar to the coherence, it is observed that for the lower frequencies, the predictions tend to be more accurate than compared to the higher frequencies. For the phase difference, the angle of attack appears to still have an influence but not as pronounced as for the coherence.

In Fig. 20, the PSD are shown for the measured and predicted signals for both the lift and pitching moment, for all tested angles of attack. The PSD of the measured and predicted signal allows us to evaluate if the relative power in the signals at different frequencies matches for the measured and predicted signal. All measured signals clearly show the peak in the frequency spectra close $f^* = 0.3$. At higher nondimensional frequencies than 0.3, the power in the signals quickly decreases. Below $f^* = 0.3$ the largest peaks in the PSD tend to be for the lower frequencies of the frequency spectra. The PSD for signals at different angles of attack show distinct frequency characteristics, with power distributed differently across the frequency spectrum. These variations indicate that the signals differ depending on the angle of attack. For the current analysis, we are primarily interested in the part of the frequency spectrum with nondimensional frequencies smaller than 0.255 to eliminate the influence on the lift and moment that could not be registered with the tufts in the current setup. It can be seen that this range of the frequency spectrum is reproduced well in the predicted signal compared to the measured signal. As was already indicated by the coherence plot, the match between the measured and predicted signal tends to be better for lower angles of attack.

In Fig. 21, samples are shown of the measured signal and the predicted signal for both the lift and pitching moment coefficient fluctuations, for all tested angles of attack. Each plot shows the 120 Hz sub-sampled measured wing loading fluctuations with gray dots. The gray line shows the same data as the gray dots but with all frequencies above $f^* = 0.255$ cutoff. The colored line in each plot shows the predicted lift coefficient (blue) or pitching moment coefficient (orange) fluctuations. Since the models predict fluctuations, the mean of the outputs should be zero

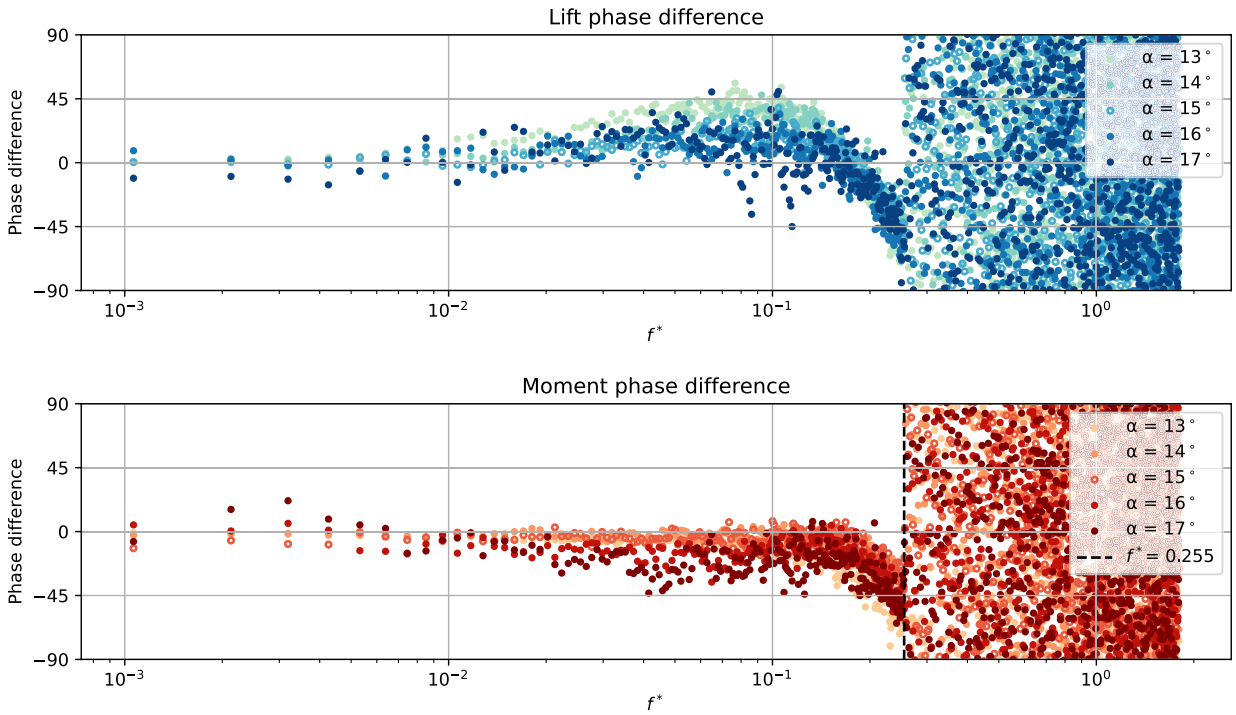

Fig. 19 The phase difference between the predicted signal and the experimentally measured signal, for both the lift and pitching moment. Angle of attack 15° represents the training data. The range for the phase difference is limited to ±90 for visual clarity

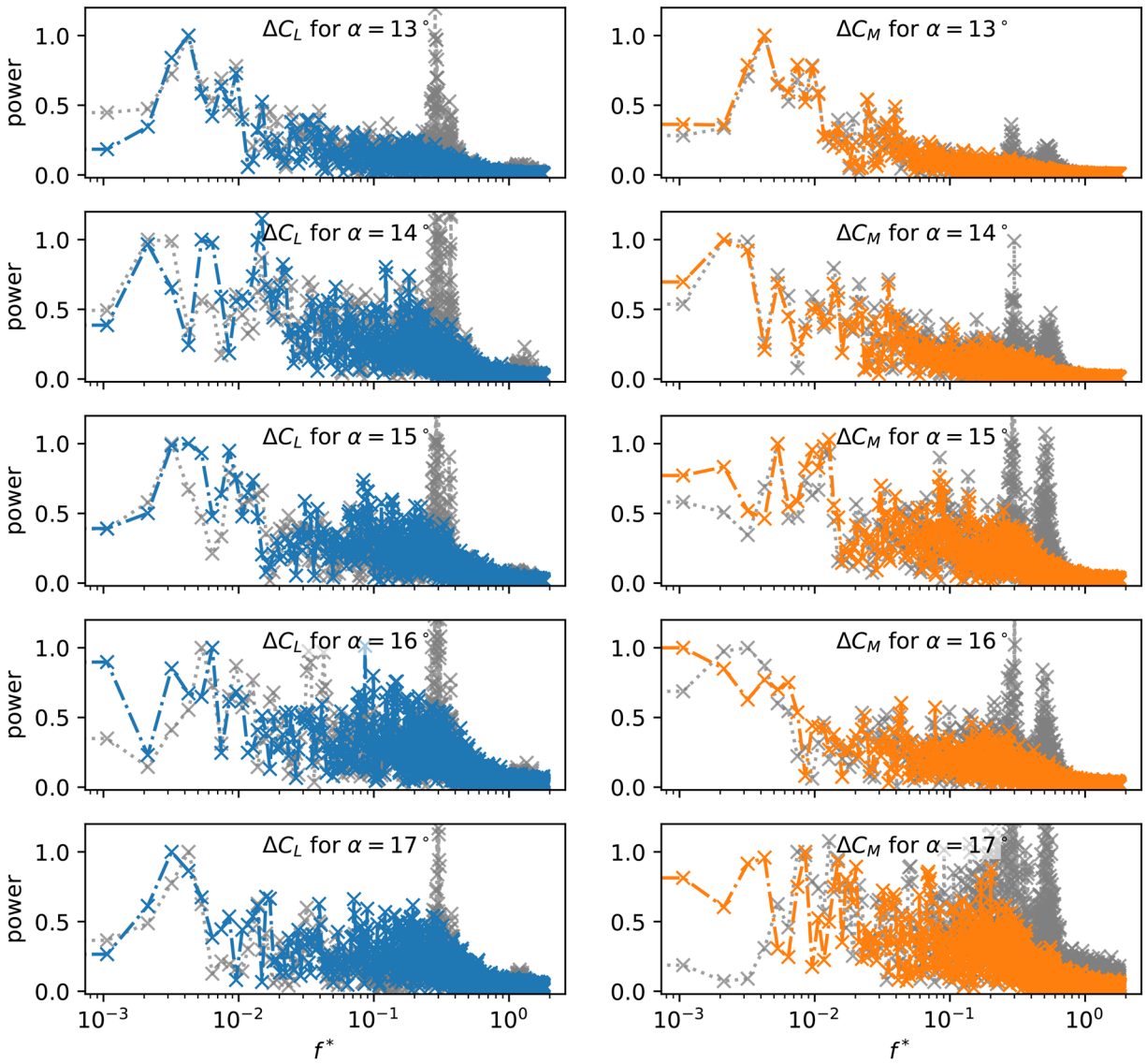

Fig. 20 The frequency spectra for the lift and moment fluctuations at different angles of attack. The original frequency spectra of the 120 Hz ($f^* = 3.6$) sub-sampled lift and pitching moment data are shown in gray. The frequency spectra of the predicted lift fluctuations are shown in blue (left column). The frequency spectra of the predicted pitching moment fluctuations are shown in orange (right column). All frequency spectra have been normalized with the maximum value of the low-frequency peak

for a series of input samples that is large enough to have a converged mean lift or pitching moment coefficient. The mean of the series of predicted outputs can be subtracted to improve the accuracy if it is known that the number of samples is large enough to represent a converged mean for the measured signal. It has already been shown that with limited pressure sensors in combination with a data-driven model, it is possible to estimate the angle of attack and Reynolds number (Zhou et al 2021). A similar approach could likely be used to estimate the mean lift and pitching moment coefficient at a given angle of attack and Reynolds number. A more in-depth investigation can evaluate if these methods work well together to offer a complete data-driven method to determine the aerodynamic loading from proxy sensors.

The fluctuations of the lift and pitching moment coefficients as shown in Fig. 21 illustrate the differences and similarities between the aerodynamic force fluctuations for different angles of attack and surface flow scenarios. For angle of attack 13° , the surface flow was highly unsteady spatially, with flow separation on the wing surface that did not take up the entire wing surface. The movement and changes in size of this separated flow area are likely correlated to the changes in aerodynamic forces on the wing. These relations are captured by the models. For angle of attack 14° , the separated flow region is larger, limiting its

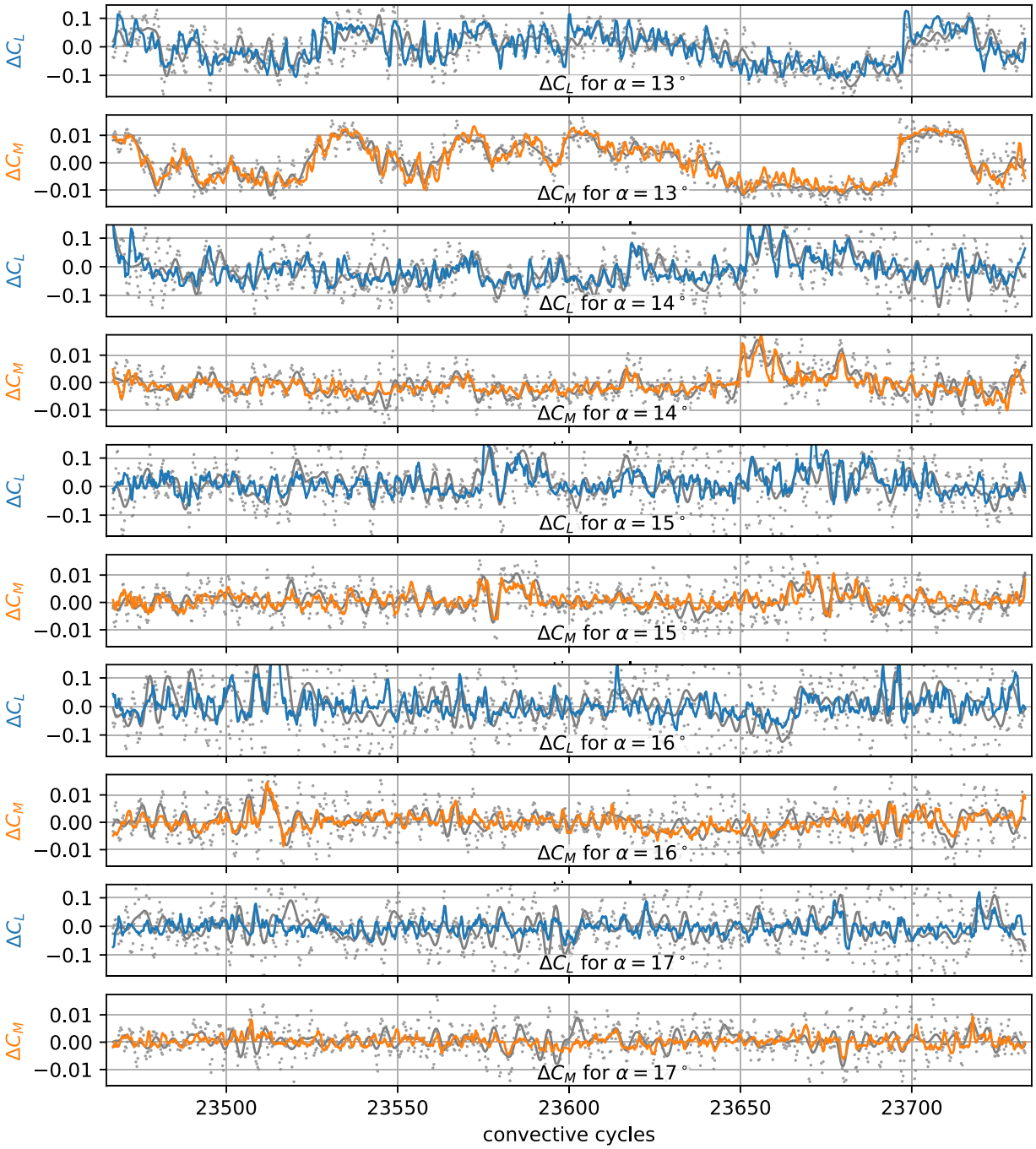

Fig. 21 The predicted lift (blue) and pitching moment coefficient (orange) fluctuations, compared to the original measurements (gray dots), and the original measurements truncated at 8.5 Hz or $f^* = 0.255$ (gray lines). The time frame shown occurs near the end of the tested time frame for each angle of attack, for angle of attack 15° this corresponds to a section from the validation data

ability to intermittently expand or to shift its position. This results in less significant long timescale (25+ convective cycles) fluctuations. For angle of attack 15° ,the separated flow area occupies the entire wing span, and shows a consistent stall cell pattern. This case was used as the training data. The higher angles of attack (16° and 17°) intermittently show full separation on the wing surface. These cases with angles of attack 16° and 17° are the cases which showed low coherence compared to the cases with angles of attack 13°, 14° and 15°. While the models were only

trained on angle of attack 15° with large areas of separated flow, the models extrapolate well to a lower angle of attack with smaller separated surface flow patterns.

5 Conclusions

In this work, both computational and experimental demonstrations have shown the potential of combining tufts with data-driven methods to provide quantitative estimates of unsteady wing loading.

A single neural network architecture with two dense layers was employed as a data-driven surrogate model for unsteady wing loading based on tuft orientations. Three distinct models were developed: one for the lift coefficient fluctuations in the computational data, another for the lift coefficient fluctuations in the experimental data, and a third for the moment coefficient fluctuations in the experimental data. Each model utilized the sine and cosine of the tuft angles as inputs.

The computational data comprised varying combinations of angle of attack and Reynolds number from URANS simulations of a 3D wing with a NACA0012 airfoil profile. Most of these simulated α-Re combinations exhibited unsteady surface flow with corresponding unsteady wing loading. Pseudo tufts were derived from the flow direction near the wing surface. The computational lift coefficient model was trained on a variety of angles of attack and Reynolds numbers and tested on several different combinations containing separated flow.

The computational data are largely free from noise, with unsteady lift fluctuations containing a limited number of peaks at specific frequencies in the power spectral density. The model is able to formulate a relation between the clearly defined surface flow patterns by the tufts and the corresponding lift fluctuations. The model can effectively interpolate between different angles of attack and Reynolds numbers, by interpolating between the observed surface flows during training at different angles of attack and Reynolds numbers.

The experimental data involved five different angles of attack at a constant Reynolds number, with simultaneous measurements of lift, moment, and tuft recordings. This data contained noise, a large variety of surface flow patterns and a broad frequency content in the lift and moment fluctuations. The experimental lift and moment coefficient models were trained on a single angle of attack and tested on four different angles of attack to evaluate the generalization ability of the surrogate model. These models showed a strong ability to generalize to different surface flow patterns across various angles of attack. The coherence between the measured and predicted signal showed that lower angles of attack tend to be predicted better. The lower end of the applicable frequency spectrum ($f^* < 0.01$) also tends to be predicted better than the higher end of the frequency spectrum ($0.01 < f^* < 0.255$). Similarly, the phase difference between the measured and predicted signal tends to be smaller for lower frequencies.

The current method has shown be suitable to predict the lift and moment coefficient fluctuations based on the surface flow patterns observed with tufts. In the future, it would be desirable to further include methods which are able to estimate the angle of attack, Reynolds number, and steady wing loading. These methods can be based on a minimal set of sensors to provide the necessary information to develop a robust method for obtaining unsteady aerodynamic loading under operational conditions.

Appendix

In Figs. 22 and 23, the frequency spectra are shown of 11 spanwise adjacent tufts near the center of the chord, for the cosine and the sine of the tuft angles, respectively. These tufts consider some locations which are prone to showing attached flow as well as tufts which tend to be inside a stall cell with separated flow. While the analysis of the specific individual tuft behavior in relation to the surface flow is outside of the scope of the current investigation, it remains relevant to assess the range of frequencies which can be found in the tuft data which is used as an input for the data-driven method with a neural network. In Fig. 22, it can be observed that the peak power of the individual tuft angle cosine frequency spectra is found between 0.1 and 1 Hz. The cosine of the tuft angle indicates the chordwise flow direction, large changes in the cosine can thus represent the switch between attached flow aligned with the freestream or separated flow going upstream near the wing surface. In Fig. 23, the frequency spectra of the sine of the tuft angles are shown, which indicate that no clear peak values are present in the frequency spectra. The sine of the tuft angle represents the change in spanwise flow direction. It can be observed that for the spanwise flow unsteadiness, the relevant frequencies are an order of magnitude larger than for the chordwise flow unsteadiness (as represented by the cosine of the tuft angles). It appears that the $f* = 0.3$ (10 Hz) frequency peak as found in the lift and pitching moment data is also present in the spanwise fluctuations but not with a clear distinct peak value. The analysis of the tuft fluctuations as presented through the frequency spectra of the sine and cosine of the tuft angles neglects the important aspect of the magnitude of the fluctuations, which is likely important in the physical analysis of the flow. Future investigations may focus on the complete combination of the tuft angle frequency spectra and the magnitude of the tuft angle fluctuations to improve the knowledge of separated flow structures.

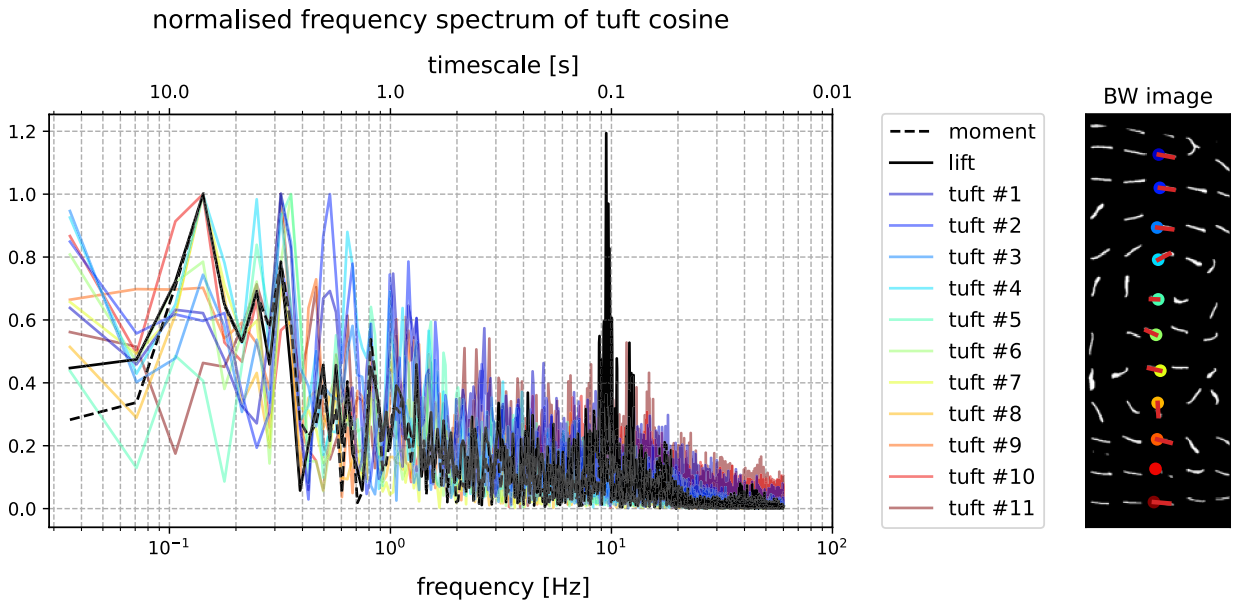

Fig. 22 Frequency spectrum comparison of different tufts at a similar chordwise position along the span. The frequency spectrum considers the variation of the cosine of the tuft angles, which is equivalent to the tuft fluctuations in chordwise direction

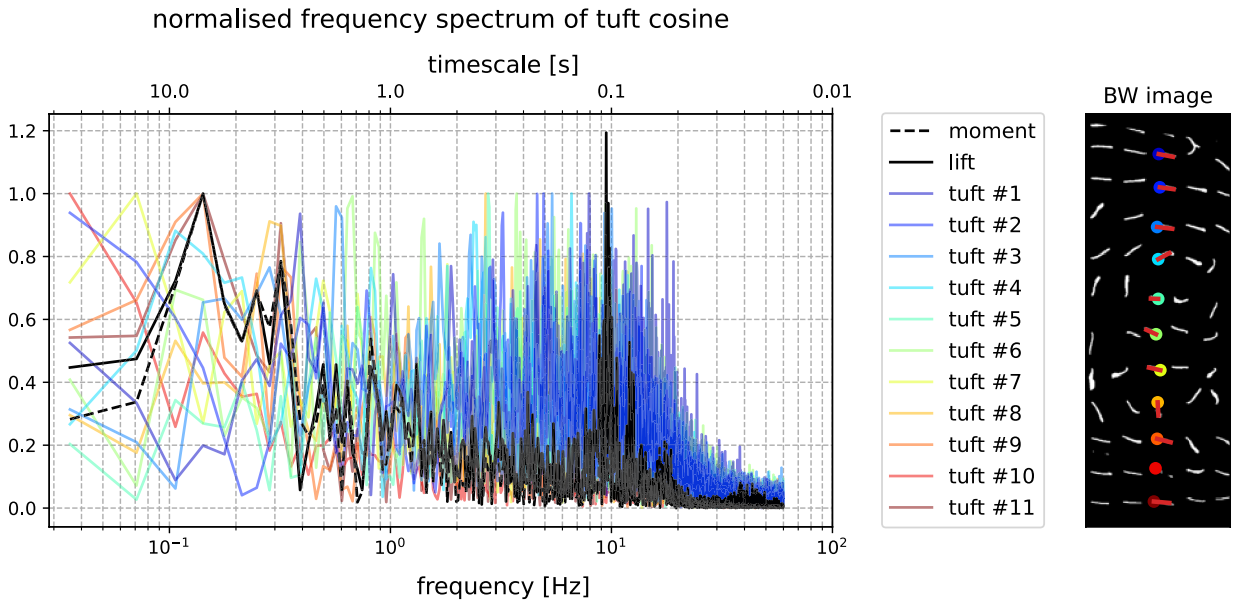

Fig. 23 Frequency spectrum comparison of different tufts at a similar chordwise position along the span. The frequency spectrum considers the variation of the sine of the tuft angles, which is equivalent to the tuft fluctuations in spanwise direction

Author Contributions Conceptualization was contributed by F.D.V. and B.G.; investigation and writing original draft were involved by F.D.V.

Funding The authors gratefully acknowledge funding from H2020 Project HOMER (project No.769237) and EPSRC (grant ref. EP/R010900/1). Additionally, the authors gratefully acknowledge the use of the IRIDIS High Performance Computing Facility at the University of Southampton in the completion of this work.

Data availability Code containing the plots and the presented methodologies will be made available upon publication at https://doi.org/10.5258/SOTON/D3232.

Declarations

Conflict of interest The authors have no conflict of interest to declare that are relevant to the content of this article.

References

Bartl J, Sagmo K, Bracchi T et al (2019) Performance of the NREL S826 airfoil at low to moderate Reynolds numbers—a reference experiment for CFD models. Eur J Mech/ B Fluids 75:180–192. https://doi.org/10.1016/j.euromechflu.2018.10.002

Broeren A, Bragg M (2001) Spanwise variation in the unsteady stalling flowfields of two-dimensional airfoil models. AIAA J 39(9):1641–1651. https://doi.org/10.2514/3.14912

Cai C, Zuo Z, Liu S et al (2018) Effect of a single leading-edge protuberance on NACA 63_4-021 airfoil performance. J Fluids Eng 140(2):021108. https://doi.org/10.1115/1.4037980

Chen L, Suzuki T, Nonomura T et al (2019) Characterization of luminescent mini-tufts in quantitative flow visualization experiments: Surface flow analysis and modelization. Exp Thermal Fluid Sci 103:406–417. https://doi.org/10.1016/j.expthermflusci.2019.02.002

Chen L, Suzuki T, Nonomura T et al (2020) Flow visualization and transient behavior analysis of luminescent mini-tufts after a backward-facing step. Flow Meas Instrum. https://doi.org/10.1016/j.flowmeasinst.2019.101657

Crow S (1970) Stability theory for a pair of trailing vortices. AIAA J 8(12):2172–2179. https://doi.org/10.2514/3.6083

De Voogt F, Ganapathisubramani B (2022) Effects of a trailing-edge flap on stall cell characteristics of a NACA0012 wing. Flow. https://doi.org/10.1017/flo.2022.11

Dell'Orso H, Amitay M (2018) Parametric investigation of stall cell formation on a NACA 0015 airfoil. AIAA J 56(8):3216–3228. https://doi.org/10.2514/1.J056850

Engelberg S (2008) Digital signal processing: an experimental approach. Springer, London. https://doi.org/10.1007/978-1-84800-119-0

Galamhos C, Matas J, Kittler J (1999) Progressive probabilistic hough transform for line detection. In: Proceedings 1999 IEEE Computer Society Conference on Computer Vision and Pattern Recognition 1:554–560. https://doi.org/10.1109/CVPR.1999.786993

Gregory N, O'Reilly C (1970) Low-Speed Aerodynamic Characteristics of NACA 0012 Aerofoil Section, including the Effects of Upper-Surface Roughness Simulating Hoar Frost. Aeronautical Research Council: Reports and Memoranda (3726)

Kingma DP, Ba J (2014) Adam: a method for stochastic optimization. arXiv preprint arXiv:1412.6980

Liu D, Nishino T (2018) Numerical analysis on the oscillation of stall cells over a NACA 0012 aerofoil. Comput Fluids 175:246–259. https://doi.org/10.1016/j.compfluid.2018.08.016

Manni L, Nishino T, Delafin PL (2016) Numerical study of airfoil stall cells using a very wide computational domain. Comput Fluids 140:260–269. https://doi.org/10.1016/j.compfluid.2016.09.023

Manolesos M, Papadakis G, Voutsinas S (2014) An experimental and numerical investigation on the formation of stall-cells on airfoils. J Phys: Conf Ser. https://doi.org/10.1088/1742-6596/555/1/012068

Manolesos M, Papadakis G, Voutsinas S (2014) Experimental and computational analysis of stall cells on rectangular wings. Wind Energy 17(6):939–955. https://doi.org/10.1002/we.1609

Moss G, Murdin P (1968) Two-dimensional low-speed tunnel tests on the naca 0012 section including measurements made during pitching oscillations at the stall. Aeronautical Research Council: Current Papers 1145

Neves AF, Lawson NJ, Bennett CJ et al (2020) Unsteady aerodynamics analysis and modelling of a slingsby firefly aircraft: Detached-eddy simulation model and flight test validation. Aerosp Sci Technol 106(106):179. https://doi.org/10.1016/j.ast.2020.106179

Nuttall A (1981) Some windows with very good sidelobe behaviour. IEEE Trans Acoust Speech Signal Process 29(1):84–91. https://doi.org/10.1109/TASSP.1981.1163506

Schewe G (2001) Reynolds-number effects in flow around more-or-less bluff bodies. J Wind Eng Ind Aerodyn 89(14–15):1267–1289. https://doi.org/10.1016/S0167-6105(01)00158-1

Steinfurth B, Cura C, Gehring J et al (2020) Tuft deflection velocimetry: a simple method to extract quantitative flow field information. Exp Fluids. https://doi.org/10.1007/s00348-020-02979-7

Swytink-Binnema N, Johnson D (2016) Digital tuft analysis of stall on operation wind turbines. Wind Energy 19:703–715. https://doi.org/10.1002/we.1860

Vey S, Lang H, Nayeri C et al (2014) Extracting quantitative data from tuft flow visualizations on utility scale wind turbines. J Phys: Conf Ser. https://doi.org/10.1088/1742-6596/524/1/012011

Weihs D, Katz J (1983) Cellular patterns in poststall flow over unswept wings. AIAA J 21(12):1757–1759. https://doi.org/10.2514/3.8321

Yon S, Katz J (1998) Study of the unsteady flow features on a stalled wing. AIAA J 36(3):305–312. https://doi.org/10.2514/2.372

Zhou K, Zhou L, Zhao S et al (2021) Data-driven method for flow sensing of aerodynamic parameters using distributed pressure measurements. AIAA J. https://doi.org/10.2514/1.J060118